

## Nondipole signatures in ionization and high-order harmonic generation

M. C. Suster<sup>✉,\*</sup>, J. Derlikiewicz<sup>✉,†</sup>, K. Krajewska, F. Cajiao Vélaz<sup>✉,‡</sup>, and J. Z. Kamiński<sup>✉</sup>  
*Institute of Theoretical Physics, Faculty of Physics, University of Warsaw, Pasteura 5, 02-093 Warsaw, Poland*

 (Received 27 November 2022; revised 16 February 2023; accepted 2 May 2023; published 16 May 2023)

We analyze nondipole effects arising in ionization and high-order harmonic generation for a two-dimensional hydrogen atom irradiated with either low- or high-frequency laser pulses. In the low-frequency case, the electron wave packet dynamics is dominated by rescattering processes within the laser pulse. Here both odd- and even-order harmonics are generated in the direction of the laser field propagation and polarization, respectively. For high-frequency pulses, such rescattering processes can be neglected. We demonstrate that a significant portion of photoelectrons is detected opposite to the laser pulse propagation direction as a consequence of their postpulse wave packet spreading and interaction with the parent ion. This is accompanied by rich interference structures formed in the momentum distributions of photoelectrons. Our results follow from the numerical solution of the time-dependent Schrödinger equation, which is based on the Suzuki-Trotter scheme with the split-step Fourier approach. The method relies on a Hamiltonian decomposition, where except for the components depending exclusively on the momentum or on the position operators, there are also terms depending on both momentum and position operators in particular configurations. We demonstrate that, as long as the latter does not depend on noncommuting coordinates of the momentum and position operators, nondipole effects in laser-matter interactions can be studied without applying extra approximations and unitary operations.

DOI: [10.1103/PhysRevA.107.053112](https://doi.org/10.1103/PhysRevA.107.053112)

### I. INTRODUCTION

With the construction of the laser, scientists acquired an exceptional tool to generate coherent and intense beams of light. This source of radiation allows the observation of highly nonlinear phenomena such as above-threshold ionization (ATI) [1] or high-order harmonic generation (HHG) [2]. In these processes, the electron interaction with the electromagnetic radiation is comparable in strength to the binding Coulomb forces inside the atom. Hence, the traditionally used perturbation theory is not applicable to the description of such processes. Novel theoretical approaches were therefore developed, including the strong-field approximation (SFA) in ATI [3–5], the semiclassical three-step model [6–10], and the Lewenstein model in HHG [11]. In the SFA the exact electron scattering state is approximated by the Volkov state in the laser field [12], i.e., the Coulomb interaction is neglected once the electron is promoted to the continuum. Such an approximation is fully justified in high-energy ionization of neutral atoms (when the Born approximation for the final scattering state can be applied) or in photodetachment from negative ions (as discussed in Refs. [13–16]). However, at low photoelectron energies or when the initial target is a positively charged ion, the Coulomb interaction modifies the electron evolution importantly. Similarly, the Lewenstein model considers a free electron moving under the action of the electric field during its excursion to the continuum and before it recombines with

the parent ion. It is the recombination process that leads to the emission of photons with energies that are integer multiples of the driving photon's energy, provided the laser pulse is sufficiently long.

With the development of modern computers, another approach, arising from the first principles of quantum mechanics, was established. This is by solving numerically the time-dependent Schrödinger equation (TDSE). It is typically based on the application of the finite-difference method and the Crank-Nicolson propagator while space and time variables are discretized [17]. This approach was used to analyze quantum effects in diverse scattering processes [17–20], to explore the ATI from hydrogen [21], and to study multiphoton ionization in a one-dimensional atomic model [22]. Other propagation methods include the Peaceman-Rachford method (see Refs. [23–25] and references therein) and the Suzuki-Trotter approach [26–30], among others. Contrary to the SFA, the numerical solution of the TDSE does not offer analytical expressions for the probability amplitudes and requires substantial computational effort, particularly when projecting the exact scattering state onto the field-free eigenstates of the atomic Hamiltonian. Nevertheless, the TDSE offers an accurate description of quantum effects (for some limited laser pulse parameters) including rescattering, spreading of the electron wave packet, and Coulomb modifications of the electron trajectories. For this reason, this *ab initio* method is particularly useful in describing ionization from atoms or positively charged ions or in analyzing processes where the above-mentioned quantum signatures are important.

In order to reduce the complexity of the above theoretical methods, the dipole approximation is typically used. In this approximation, while the laser field varies in time, it is

\*Mihai.Suster@fuw.edu.pl

†Julia.Derlikiewicz@fuw.edu.pl

‡Felipe.Cajiao-Velez@fuw.edu.pl

homogeneously distributed in space [31] (i.e., the laser field does not propagate). This is justified provided the wavelength of the laser wave is considerably larger than the dimensions of atomic targets and so it breaks down for high-frequency fields. In addition, the influence of the magnetic component of the laser pulse on the electron dynamics has to be negligible compared to that of the electric field. This in turn is satisfied for driving fields with low to moderate intensities. Note that in ionization by ultraintense laser pulses the magnetic field plays an important role in the evolution of the electron wave packet [32–37]. Also, the assumption of nonpropagating laser fields and the absence of a magnetic component render impossible the treatment of effects such as radiation pressure, where photons transfer momentum to the system in the direction of field propagation [38,39]. Furthermore, it has been shown both experimentally and theoretically (see Refs. [40–42] and references therein) that photoionization by near-infrared laser pulses of moderate intensities already exhibits signatures of radiation pressure. This imposes a low-frequency limit on the applicability of the dipole approximation.

With the invention of the chirped-pulse amplification technique by Strickland and Mourou [43] and with the development of free-electron lasers (FELs), extremely intense laser pulses with frequencies ranging from the x-ray regime down to the infrared regime could be obtained. For instance, in the HERCULES project, a 300-TW Ti:sapphire laser pulse is tightly focused such that an intensity of  $I \sim 2 \times 10^{22}$  W/cm<sup>2</sup> can be achieved [44,45]. In addition, x-ray FELs can produce coherent pulses of radiation with wavelengths down to  $\lambda \sim 0.1$  nm and intensities  $I \sim 1 \times 10^{20}$  W/cm<sup>2</sup> [46]. Also, intense laser pulses in the long-wave infrared regime have been obtained, with wavelengths of the order of  $\lambda \sim 9$   $\mu$ m [47]. It is clear that laser-matter interactions in those high- or low-frequency and high-intensity regimes are beyond the applicability of the dipole approximation.

Signatures of radiation pressure have been observed in ionization by high-intensity long-wavelength laser pulses. Such signatures appear as asymmetries in angular distributions of photoelectrons in the direction of laser field propagation [40,48–50] (i.e., ionized electrons are detected with an additional momentum in that direction). Interestingly, under certain circumstances, a combination of Coulomb focusing and nondipole effects in elliptically polarized fields leads to a shift of the photoelectron distribution towards the laser source [48,49,51] (see also Ref. [52]). Further, in photoionization by ultraintense laser pulses important relativistic effects take place. For this reason, the electron dynamics should be described by the Dirac or Klein-Gordon equations rather than by the Schrödinger equation. To this end, the relativistic strong-field approximation [53] makes use of the relativistic Volkov solution [12] while accounting for effects such as radiation pressure and spin dynamics. It is also possible to introduce certain corrections in the expressions derived from the original SFA in order to account for relativistic effects. Such an approach is known as the quasirelativistic SFA [54,55]. Among those corrections we mention (i) recoil or higher-order Nordsieck corrections [56], which account for radiation pressure effects, (ii) retardation correction, which reflects the fact that the laser field is a propagating wave, and (iii) relativistic mass correction, related to the relativistic

variation of the electron mass. Thus, it is possible to account for nondipole effects within the nonrelativistic framework. Other approaches, which have been successfully applied to analyze nondipole effects in both ATI [57–59] and HHG [60], consist in formulating an asymptotic solution of the Coulomb-free Schrödinger equation outside the dipole approximation. In such cases, the continuum states in the SFA (modified Volkov solutions) contain important nondipole signatures (see also the derivations in Refs. [61–65] for electron scattering and atomic motion in multimode laser fields). Moreover, the nondipole dynamics in tunneling ionization was recently studied in [66,67] and the strong-field ionization of atoms by an elliptically polarized laser field was discussed in [68]. We note that nondipole effects have also been analyzed in few-photon ionization under the framework of the perturbation theory and the numerical solution of TDSE (see, e.g., [69–71]). Other theoretical approaches, including classical analysis in conjunction with the Monte Carlo method, were thoroughly discussed in the review article in [72].

The plan of this paper is as follows. In Sec. II we introduce the analytical framework together with the algorithm employed in our investigation. In Sec. III A we describe the two-dimensional Coulomb-like central potential used to model the target atom. Section III B relates to the Hamiltonian decomposition for the Suzuki-Trotter method, in both the dipole and nondipole regimes. In Sec. III C we define the laser pulse. The numerical parameters used to solve the time-dependent Schrödinger equation are presented in Sec. IV. The application of this model to describe physical phenomena is discussed in Sec. V. By introducing the mean values of position and velocity operators, we compare the electron dynamics with and without the dipole approximation. In particular, in Sec. V A the nondipole effects in HHG are explored for the low-frequency laser pulses and in Sec. V B we analyze the radiation pressure effects and forward drift of the electron wave packet in the high-frequency pulses. Section VI concerns the backward electron propagation which, according to our investigation, is a consequence of the postpulse electron wave packet spreading and its interaction with the parent ion. The convergence of the numerical scheme and the electron probability currents are studied in Sec. VII. The photoelectron momentum distributions are discussed in Sec. VIII. A summary is given in Sec. IX.

In our numerical analysis, we use the atomic units of momentum  $p_0 = \alpha m_e c$ , energy  $E_0 = \alpha^2 m_e c^2$ , length  $a_0 = \hbar/p_0$ , time  $t_0 = \hbar/E_0$ , and electric-field strength  $\mathcal{E}_0 = \alpha^3 m_e^2 c^3 / |e| \hbar$ , where  $m_e$  and  $e = -|e|$  are the electron rest mass and charge, and  $\alpha$  is the fine-structure constant. In analytical formulas we set  $\hbar = 1$  while keeping explicitly the remaining fundamental constants.

## II. THEORETICAL BACKGROUND

The dynamics of a quantum system is governed by the wave equation

$$i\partial_t |\psi(t)\rangle = \hat{H}(\hat{\mathbf{p}}, \hat{\mathbf{x}}, t) |\psi(t)\rangle, \quad (1)$$

where  $\hat{H}(\hat{\mathbf{p}}, \hat{\mathbf{x}}, t)$  is the Hamiltonian of the system under consideration, with  $\hat{\mathbf{p}}$  and  $\hat{\mathbf{x}}$  the momentum and position operators, respectively. They fulfill the Heisenberg commutation

relations

$$[\hat{x}_j, \hat{p}_\ell] = i\delta_{j\ell}, \quad j, \ell = 1, \dots, D, \quad (2)$$

where  $D$  is the spatial dimensionality of the system. Depending on the form of the Hamiltonian, Eq. (1) is called the Schrödinger, Pauli, or Dirac equation.

The time evolution of an initial state  $|\psi(t_0)\rangle$  is given by the unitary operator  $\hat{U}(t, t_0)$ ,

$$|\psi(t)\rangle = \hat{U}(t, t_0)|\psi(t_0)\rangle, \quad (3)$$

which satisfies an identical wave equation

$$i\partial_t \hat{U}(t, t_0) = \hat{H}(\hat{\mathbf{p}}, \hat{\mathbf{x}}, t) \hat{U}(t, t_0), \quad (4)$$

with the initial condition  $\hat{U}(t_0, t_0) = \hat{I}$ , where  $\hat{I}$  is the identity operator. The formal solution of this equation can be presented in the form

$$\hat{U}(t, t_0) = \hat{\mathcal{T}} \left[ \exp \left( -i \int_{t_0}^t d\tau \hat{H}(\hat{\mathbf{p}}, \hat{\mathbf{x}}, \tau) \right) \right], \quad (5)$$

where  $\hat{\mathcal{T}}$  is the Dyson time-ordering operator. As follows from this expression, the evolution operator fulfills the decomposition relation

$$\hat{U}(t, t_0) = \hat{U}(t, t') \hat{U}(t', t_0), \quad t_0 < t' < t, \quad (6)$$

which is the basis of the numerical integration of the wave equation (1). Indeed, by introducing the time discretization

$$t_n = t_0 + n\delta t, \quad n = 0, 1, \dots, N, \quad \delta t = \frac{t - t_0}{N}, \quad (7)$$

we obtain

$$\hat{U}(t, t_0) = \hat{U}(t_N, t_{N-1}) \cdots \hat{U}(t_1, t_0) = \prod_{n=0}^{N-1} \hat{U}(t_{n+1}, t_n). \quad (8)$$

For a sufficiently small time increment  $\delta t$  (or sufficiently large number of time steps  $N$ ), we can use the approximation

$$\hat{U}(t_{n+1}, t_n) = e^{-i\delta t \hat{H}(\hat{\mathbf{p}}, \hat{\mathbf{x}}, \bar{t}_n)}, \quad (9)$$

with some properly chosen  $\bar{t}_n \in [t_n, t_{n+1}]$ .

Let us further assume that the Hamiltonian is the sum of two terms

$$\hat{H}(\hat{\mathbf{p}}, \hat{\mathbf{x}}, t) = \hat{H}_1(\hat{\mathbf{p}}, \hat{\mathbf{x}}, t) + \hat{h}_2(\hat{\mathbf{p}}, \hat{\mathbf{x}}, t). \quad (10)$$

Then, as follows from the analysis presented in Refs. [26–28], we can approximate the evolution operator for infinitesimally small times  $\hat{U}(t_{n+1}, t_n)$  as

$$\hat{U}(t_{n+1}, t_n) = \hat{U}_{\text{ST2}}(t_{n+1}, t_n) + O((\delta t)^3), \quad (11)$$

where

$$\hat{U}_{\text{ST2}}(t_{n+1}, t_n) = e^{-i(\delta t/2)\hat{H}_1(\hat{\mathbf{p}}, \hat{\mathbf{x}}, \bar{t}_n)} e^{-i\delta t \hat{h}_2(\hat{\mathbf{p}}, \hat{\mathbf{x}}, \bar{t}_n)} e^{-i(\delta t/2)\hat{H}_1(\hat{\mathbf{p}}, \hat{\mathbf{x}}, \bar{t}_n)} \quad (12)$$

and  $\bar{t}_n = (t_n + t_{n+1})/2$ . Such an approximation is the essence of the Suzuki-Trotter method for the numerical solution of the TDSE.

Further, we assume that  $\hat{h}_2(\hat{\mathbf{p}}, \hat{\mathbf{x}}, t)$  also consists of two separate terms, i.e.,

$$\hat{h}_2(\hat{\mathbf{p}}, \hat{\mathbf{x}}, t) = \hat{H}_2(\hat{\mathbf{p}}, \hat{\mathbf{x}}, t) + \hat{h}_3(\hat{\mathbf{p}}, \hat{\mathbf{x}}, t). \quad (13)$$

In this case, according to the Suzuki-Trotter method, the infinitesimal evolution operator reads

$$\hat{U}(t_{n+1}, t_n) = \hat{U}_{\text{ST3}}(t_{n+1}, t_n) + O((\delta t)^3), \quad (14)$$

with

$$\begin{aligned} \hat{U}_{\text{ST3}}(t_{n+1}, t_n) &= e^{-i(\delta t/2)\hat{H}_1(\hat{\mathbf{p}}, \hat{\mathbf{x}}, \bar{t}_n)} e^{-i(\delta t/2)\hat{H}_2(\hat{\mathbf{p}}, \hat{\mathbf{x}}, \bar{t}_n)} \\ &\times e^{-i\delta t \hat{h}_3(\hat{\mathbf{p}}, \hat{\mathbf{x}}, \bar{t}_n)} e^{-i(\delta t/2)\hat{H}_2(\hat{\mathbf{p}}, \hat{\mathbf{x}}, \bar{t}_n)} \\ &\times e^{-i(\delta t/2)\hat{H}_1(\hat{\mathbf{p}}, \hat{\mathbf{x}}, \bar{t}_n)}. \end{aligned} \quad (15)$$

If desired, such a procedure can be sequentially repeated  $\mathcal{K}$  times in order to account for  $\mathcal{K}$  decompositions of the initial Hamiltonian. To identify the number of those decompositions, in Eqs. (11)–(15) we use the subscript ST $\mathcal{K}$ , with  $\mathcal{K} = 2$  or 3 and ST indicating that the Suzuki-Trotter approximation is used. Finally, from Eq. (8) we arrive at an expression for the evolution operator with the Hamiltonian decomposed into  $\mathcal{K}$  parts,

$$\hat{U}(t, t_0) = \prod_{n=0}^{N-1} \hat{U}_{\text{ST}\mathcal{K}}(t_{n+1}, t_n) + O((\delta t)^2). \quad (16)$$

Note that the overall error of this method is of the order of  $(\delta t)^2$ . It can be made smaller by applying additional corrections [28,29,73,74], in particular those proposed by Suzuki [75] and Yoshida [76]. Here it is also important to note that the approximations introduced above preserve the unitarity of the evolution operator, provided the Hamiltonian is Hermitian.

The power of the Suzuki-Trotter approximation is that the action of each exponent operator can be efficiently applied over any state of the system. For this to happen, the Hamiltonian decompositions should have some particular properties. For instance, if in Eq. (10) the operators  $\hat{H}_1$  and  $\hat{h}_2$  depend only on momentum and position operators, respectively, the fast Fourier transform algorithm [77–79] can be applied. In order to proceed further, let us denote by  $|\mathbf{x}; X\rangle$  and  $|\mathbf{p}; P\rangle$  the eigenstates of the position and momentum operators

$$\hat{\mathbf{x}}|\mathbf{x}; X\rangle = \mathbf{x}|\mathbf{x}; X\rangle, \quad \hat{\mathbf{p}}|\mathbf{p}; P\rangle = \mathbf{p}|\mathbf{p}; P\rangle, \quad (17)$$

which, in a  $D$ -dimensional space, satisfy the orthogonality and completeness relations

$$\begin{aligned} \langle \mathbf{x}'; X | \mathbf{x}; X \rangle &= \delta^{(D)}(\mathbf{x} - \mathbf{x}'), \\ \langle \mathbf{p}'; P | \mathbf{p}; P \rangle &= (2\pi)^D \delta^{(D)}(\mathbf{p} - \mathbf{p}'), \end{aligned} \quad (18)$$

$$\hat{I} = \int d^D x |\mathbf{x}; X\rangle \langle \mathbf{x}; X| = \int \frac{d^D p}{(2\pi)^D} |\mathbf{p}; P\rangle \langle \mathbf{p}; P|, \quad (19)$$

together with

$$\langle \mathbf{x}; X | \mathbf{p}; P \rangle = e^{i\mathbf{p}\cdot\mathbf{x}}. \quad (20)$$

Therefore, for any state  $|\phi\rangle$  we can write

$$\langle \mathbf{x}; X | e^{-i\delta t \hat{h}_2(\hat{\mathbf{x}}, t)} |\phi\rangle = e^{-i\delta t h_2(\mathbf{x}, t)} \langle \mathbf{x}; X | \phi \rangle \quad (21)$$

and

$$\langle \mathbf{p}; P | e^{-i\delta t \hat{H}_1(\hat{\mathbf{p}}, t)} |\phi\rangle = e^{-i\delta t H_1(\mathbf{p}, t)} \langle \mathbf{p}; P | \phi \rangle, \quad (22)$$

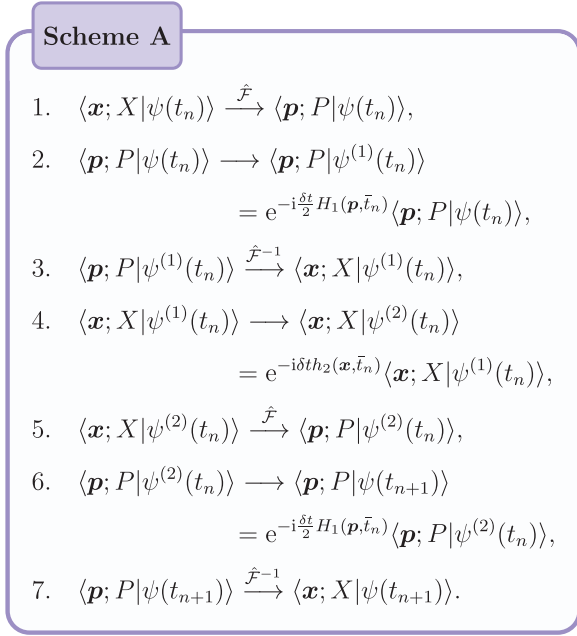


FIG. 1. Scheme A for the Suzuki-Trotter split-step Fourier method with a Hamiltonian divided into two terms [see Eq. (12)]. It is assumed that each Hamiltonian component depends either on the momentum or on the position operator [Eq. (24)] and that the wave function describing the quantum state of the system at time  $t_n$ ,  $|\psi(t_n)\rangle$ , is known. In this scheme, we illustrate the steps that lead to  $|\psi(t_{n+1})\rangle$  in position representation. Note that this type of algorithm is commonly used within the dipole approximation.

where the functions  $\langle \mathbf{x}; X|\phi\rangle$  and  $\langle \mathbf{p}; P|\phi\rangle$  are related through the Fourier transform

$$\langle \mathbf{p}; P|\phi\rangle = \int d^D x e^{-i\mathbf{p}\cdot\mathbf{x}} \langle \mathbf{x}; X|\phi\rangle. \quad (23)$$

Hence, we can determine the evolution operator given by Eqs. (11) and (12). In order to illustrate this, in Fig. 1 we show the steps for the temporal evolution of a system according to the Suzuki-Trotter split-step Fourier method (scheme A). It is assumed that such a system is originally found in the state  $|\psi(t_n)\rangle$  and that the Hamiltonian can be decomposed into two parts ( $\mathcal{K} = 2$ ). We also assume that each Hamiltonian term depends exclusively on either position or momentum operators, i.e., we write

$$\hat{H}(\hat{\mathbf{p}}, \hat{\mathbf{x}}, t) = \hat{H}_1(\hat{\mathbf{p}}, t) + \hat{h}_2(\hat{\mathbf{x}}, t). \quad (24)$$

In our notation,  $\hat{F}$  and  $\hat{F}^{-1}$  represent the Fourier transform (FT) and its inverse (IFT), respectively. Note that, by applying the procedure shown in Fig. 1, we start with the wave function  $|\psi(t_n)\rangle$  and end up with  $|\psi(t_{n+1})\rangle$ , both in the position representation.

The algorithm presented in scheme A (Fig. 1) is broadly used in strong-field physics when applying the dipole approximation (see, e.g., Refs. [38,80–83]). If, however, nondipole effects are going to be studied, this scheme has to be suitably modified. This is done by applying additional approximations, the validity of which has to be investigated. To this end, we present below an extension of this scheme toward a triply decomposed Hamiltonian ( $\mathcal{K} = 3$ ). Such an extension is based

on the approximation given by Eqs. (14) and (15). First, we assume that  $\hat{H}_1$  and  $\hat{H}_2$  in Eqs. (10) and (13) depend *only* on the momentum  $\hat{\mathbf{p}}$  and the position  $\hat{\mathbf{x}}$  operators, respectively. However, the third term  $\hat{h}_3(\hat{\mathbf{p}}, \hat{\mathbf{x}}, t)$  depends on both of them. Therefore, the full Hamiltonian  $\hat{H}(\hat{\mathbf{p}}, \hat{\mathbf{x}}, t)$  reads

$$\hat{H}(\hat{\mathbf{p}}, \hat{\mathbf{x}}, t) = \hat{H}_1(\hat{\mathbf{p}}, t) + \hat{H}_2(\hat{\mathbf{x}}, t) + \hat{h}_3(\hat{\mathbf{p}}, \hat{\mathbf{x}}, t). \quad (25)$$

It is also assumed that the term with mixed operators  $\hat{h}_3(\hat{\mathbf{p}}, \hat{\mathbf{x}}, t)$  is expressed exclusively by commuting components of  $\hat{\mathbf{p}}$  and  $\hat{\mathbf{x}}$ , i.e., it is written in a particular configuration. This configuration is defined by a multi-index  $\sigma$ ,

$$\sigma = (\sigma_1, \sigma_2, \dots, \sigma_D), \quad (26)$$

where  $\sigma_j = 0$  or 1 for  $j = 1, \dots, D$ . Introducing now the operators

$$\hat{\mathbf{x}}^\sigma = ((1 - \sigma_1)\hat{x}_1, \dots, (1 - \sigma_D)\hat{x}_D) \quad (27)$$

and

$$\hat{\mathbf{p}}^\sigma = (\sigma_1\hat{p}_1, \dots, \sigma_D\hat{p}_D), \quad (28)$$

we see that all components of  $\hat{\mathbf{x}}^\sigma$  and  $\hat{\mathbf{p}}^\sigma$  commute with each other. Moreover, the configuration  $\sigma$  defines the position and momentum vectors ( $\mathbf{x}^\sigma$  and  $\mathbf{p}^\sigma$ , respectively) such that their scalar product vanishes,  $\mathbf{p}^\sigma \cdot \mathbf{x}^\sigma = 0$ . For the purpose of our further analysis, we define also the scalar product in the  $\sigma$  configuration as

$$(\mathbf{p}^\sigma, \mathbf{x}^\sigma) = \sum_{j=1}^D \sigma_j p_j x_j = \sum_{\sigma_j=1} p_j x_j. \quad (29)$$

This allows us to introduce the partial Fourier transform, denoted by  $\hat{F}_\sigma$ , such that for any state  $|\phi\rangle$  we have

$$\langle \mathbf{x}; X|\phi\rangle \xrightarrow{\hat{F}_\sigma} \langle \mathbf{p}^\sigma, \mathbf{x}^\sigma|\phi\rangle, \quad (30)$$

with

$$\langle \mathbf{p}^\sigma, \mathbf{x}^\sigma|\phi\rangle = \int \left[ \prod_{\sigma_j=1} dx_j \right] e^{-i(\mathbf{p}^\sigma, \mathbf{x}^\sigma)} \langle \mathbf{x}; X|\phi\rangle, \quad (31)$$

which leads to the mixed position-momentum representation of a quantum state  $|\phi\rangle$ . Similarly to the relations (21) and (22), for the Hamiltonian  $\hat{h}_3(\hat{\mathbf{p}}^\sigma, \hat{\mathbf{x}}^\sigma, t)$  we arrive at

$$\langle \mathbf{p}^\sigma, \mathbf{x}^\sigma|e^{-i\delta t \hat{h}_3(\hat{\mathbf{p}}^\sigma, \hat{\mathbf{x}}^\sigma, t)}|\phi\rangle = e^{-i\delta t h_3(\mathbf{p}^\sigma, \mathbf{x}^\sigma, t)} \langle \mathbf{p}^\sigma, \mathbf{x}^\sigma|\phi\rangle. \quad (32)$$

This leads to the Suzuki-Trotter algorithm presented in scheme B (Fig. 2). Here  $\hat{F}_\sigma$  is the partial Fourier transform and  $\hat{F}_\sigma^{-1}$  is its inverse calculated in the  $\sigma$  configuration according to Eqs. (30) and (31). Note that this scheme can be easily expanded if the Hamiltonian contains more than one term in a given configuration. It has been tested by comparing its predictions with the exactly solvable model of a harmonic oscillator interacting with electric and magnetic fields [84]. In this model, the frequencies of the harmonic oscillator and both fields arbitrarily depend on time. If the initial state is a Gaussian function, then one can either find a solution of the Schrödinger equation in an analytical form or the problem can be reduced to the solution of a system of ordinary differential equations.

**Scheme B**

1.  $\langle \mathbf{x}; X|\psi(t_n)\rangle \xrightarrow{\hat{F}} \langle \mathbf{p}; P|\psi(t_n)\rangle$ ,
2.  $\langle \mathbf{p}; P|\psi(t_n)\rangle \rightarrow \langle \mathbf{p}; P|\psi^{(1)}(t_n)\rangle$   
 $= e^{-i\frac{\delta t}{2}H_1(\mathbf{p},\bar{t}_n)}\langle \mathbf{p}; P|\psi(t_n)\rangle$ ,
3.  $\langle \mathbf{p}; P|\psi^{(1)}(t_n)\rangle \xrightarrow{\hat{F}^{-1}} \langle \mathbf{x}; X|\psi^{(1)}(t_n)\rangle$ ,
4.  $\langle \mathbf{x}; X|\psi^{(1)}(t_n)\rangle \rightarrow \langle \mathbf{x}; X|\psi^{(2)}(t_n)\rangle$   
 $= e^{-i\frac{\delta t}{2}H_2(\mathbf{x},\bar{t}_n)}\langle \mathbf{x}; X|\psi^{(1)}(t_n)\rangle$ ,
5.  $\langle \mathbf{x}; X|\psi^{(2)}(t_n)\rangle \xrightarrow{\hat{F}_\sigma} \langle \mathbf{p}^\sigma, \mathbf{x}^\sigma|\psi^{(2)}(t_n)\rangle$ ,
6.  $\langle \mathbf{p}^\sigma, \mathbf{x}^\sigma|\psi^{(2)}(t_n)\rangle \rightarrow \langle \mathbf{p}^\sigma, \mathbf{x}^\sigma|\psi^{(3)}(t_n)\rangle$   
 $= e^{-i\delta t h_3(\mathbf{p}^\sigma, \mathbf{x}^\sigma, \bar{t}_n)}\langle \mathbf{p}^\sigma, \mathbf{x}^\sigma|\psi^{(2)}(t_n)\rangle$ ,
7.  $\langle \mathbf{p}^\sigma, \mathbf{x}^\sigma|\psi^{(3)}(t_n)\rangle \xrightarrow{\hat{F}_\sigma^{-1}} \langle \mathbf{x}; X|\psi^{(3)}(t_n)\rangle$ ,
8.  $\langle \mathbf{x}; X|\psi^{(3)}(t_n)\rangle \rightarrow \langle \mathbf{x}; X|\psi^{(4)}(t_n)\rangle$   
 $= e^{-i\frac{\delta t}{2}H_2(\mathbf{x},\bar{t}_n)}\langle \mathbf{x}; X|\psi^{(3)}(t_n)\rangle$ ,
9.  $\langle \mathbf{x}; X|\psi^{(4)}(t_n)\rangle \xrightarrow{\hat{F}} \langle \mathbf{p}; P|\psi^{(4)}(t_n)\rangle$ ,
10.  $\langle \mathbf{p}; P|\psi^{(4)}(t_n)\rangle \rightarrow \langle \mathbf{p}; P|\psi(t_{n+1})\rangle$   
 $= e^{-i\frac{\delta t}{2}H_1(\mathbf{p},\bar{t}_n)}\langle \mathbf{p}; P|\psi^{(4)}(t_n)\rangle$ ,
11.  $\langle \mathbf{p}; P|\psi(t_{n+1})\rangle \xrightarrow{\hat{F}^{-1}} \langle \mathbf{x}; X|\psi(t_{n+1})\rangle$ .

FIG. 2. Scheme B for the Suzuki-Trotter split-step Fourier method with a Hamiltonian divided into three terms [see Eq. (15)]. It is assumed that the first term  $\hat{H}_1(\hat{\mathbf{p}}, t)$  and the second term  $\hat{H}_2(\hat{\mathbf{x}}, t)$  depend on the momentum and position operators, respectively. However, the third component  $\hat{h}_3(\hat{\mathbf{p}}^\sigma, \hat{\mathbf{x}}^\sigma, t)$  contains mixed operators and it is presented in the  $\sigma$  configuration [see Eqs. (27) and (28)]. While  $\hat{F}$  and  $\hat{F}^{-1}$  represent the FT and IFT,  $\hat{F}_\sigma$  and  $\hat{F}_\sigma^{-1}$  are the partial Fourier transform and its inverse in the  $\sigma$  configuration, respectively [Eqs. (30) and (31)].

In closing this section we note that a similar approach has been used recently in Refs. [85,86].

### III. PHYSICAL SYSTEM

Our aim is to investigate the nondipole signatures in ionization and high-order harmonic generation by strong laser pulses. For this purpose, we are going to apply the numerical schemes A and B presented in Sec. II to solve the one-electron Schrödinger equation. When solving the TDSE numerically, calculations are always limited to finite regions. However, in order to avoid the occurrence of unphysical reflection effects from boundaries, this area should be large enough and some absorbing boundary conditions should be imposed. This significantly affects the memory being used and the computation time. For this reason, the theoretical analysis is often limited to one- (1D) or two-dimensional (2D) spaces. Since nondipole effects (attributed to the presence of the magnetic field) do not occur in 1D spaces, we investigate ionization and high-order harmonic generation of a single-electron atom in two dimensions.

#### A. Atomic system

Let us consider a 2D hydrogenlike atom with a binding soft-core Coulomb potential

$$V(\mathbf{x}) = -\frac{\mathcal{Z}}{\sqrt{x^2 + a^2} \exp(-x/a)}, \quad (33)$$

where  $\mathcal{Z}$  is the atomic number,  $\mathbf{x} = (x_1, x_2)$  is the two-dimensional position vector, and  $x = |\mathbf{x}| = \sqrt{x_1^2 + x_2^2}$  represents its norm. To avoid the presence of quadrupole and higher multipole terms, we have introduced the exponential term  $a^2 \exp(-x/a)$  in the denominator of Eq. (33) ( $a > 0$ ). Note that in our model  $V(\mathbf{x})$  tends asymptotically to the pure Coulomb potential for large  $x$ ,

$$V(\mathbf{x}) = -\frac{\mathcal{Z}}{x} + O\left(\frac{e^{-x/a}}{x^3}\right). \quad (34)$$

Setting  $a = 1.10609a_0$  and  $\mathcal{Z} = 1$ , the ground-state energy in the potential (33) turns out to be identical to that for a 3D hydrogen atom,  $E_B = -0.5E_0$ . Moreover, the ground-state wave function  $\psi_B(\mathbf{x})$  is determined by applying either the shooting method for the radial differential equation or the Feynman-Kac method for imaginary times. Both approaches give nearly the same results for  $E_B$  and  $\psi_B(\mathbf{x})$ . Then the function  $\psi_B(\mathbf{x})$  is used as the initial state for the time propagation of the Schrödinger equation (1) with the atomic Hamiltonian

$$\hat{H}_{\text{at}}(\hat{\mathbf{p}}, \hat{\mathbf{x}}) = \frac{1}{2m_e} \hat{\mathbf{p}}^2 + V(\hat{\mathbf{x}}). \quad (35)$$

As we have checked, by choosing  $\delta t = 0.01t_0$  in scheme A (Fig. 1), the state  $\psi_B(\mathbf{x})$  acquires the phase factor  $\exp(-iE_B t)$  for  $0 < t < 100t_0$ . Thus,  $\psi_B(\mathbf{x})$  is in fact the eigenstate of the atomic Hamiltonian (35) with eigenvalue  $E_B$ .

#### B. Hamiltonian decomposition

The electron interaction with the laser field is accounted for by applying the standard minimal coupling prescription

$$\hat{H}(\hat{\mathbf{p}}, \hat{\mathbf{x}}, t) = \frac{1}{2m_e} [\hat{\mathbf{p}} - e\mathbf{A}(\hat{\mathbf{x}}, t)]^2 + V(\hat{\mathbf{x}}), \quad (36)$$

where  $e$  is the electron charge and the vector potential  $\mathbf{A}(\hat{\mathbf{x}}, t)$  describes the laser pulse. For our numerical illustrations we choose

$$\mathbf{A}(\hat{\mathbf{x}}, t) = [A(t - \hat{x}_2/c), 0], \quad (37)$$

which corresponds to a laser pulse propagating in the  $x_2$  direction and polarized linearly in the  $x_1$  direction. Hence, the total Hamiltonian in Eq. (36) can be written in the form

$$\hat{H}(\hat{\mathbf{p}}, \hat{\mathbf{x}}, t) = \hat{H}_1(\hat{\mathbf{p}}, t) + \hat{H}_2(\hat{\mathbf{x}}, t) + \hat{h}_3(\hat{\mathbf{p}}^\sigma, \hat{\mathbf{x}}^\sigma, t), \quad (38)$$

with

$$\hat{H}_1(\hat{\mathbf{p}}, t) = \frac{1}{2m_e} \hat{\mathbf{p}}^2, \quad \hat{H}_2(\hat{\mathbf{x}}, t) = \frac{1}{2m_e} [eA(t - \hat{x}_2/c)]^2 + V(\hat{\mathbf{x}}), \quad (39)$$

and

$$\hat{h}_3(\hat{\mathbf{p}}^\sigma, \hat{\mathbf{x}}^\sigma, t) = -\frac{e}{m_e} A(t - \hat{x}_2/c) \cdot \hat{p}_1. \quad (40)$$

This means that, according to our classification,  $\hat{h}_3$  is in the configuration  $\sigma = (1, 0)$ ; thus, the numerical scheme B (Fig. 2) can be applied. In contrast, in the dipole approximation, the operator  $A(t - \hat{x}_2/c)$  is replaced by the function  $A(t)$ . In this case, the Hamiltonian (36) becomes

$$\hat{H}_d(\hat{\mathbf{p}}, \hat{\mathbf{x}}, t) = \frac{1}{2m_e} \{ [\hat{p}_1 - eA(t)]^2 + \hat{p}_2^2 \} + V(\hat{\mathbf{x}}), \quad (41)$$

which defines the splitting required for the application of scheme A.

To account for nondipole corrections in the lowest order, we make an approximation

$$A(t - \hat{x}_2/c) = A(t) + \frac{1}{c} \hat{x}_2 \mathcal{E}(t) + O(1/c^2), \quad (42)$$

where  $\mathcal{E}(t) = -\dot{A}(t)$  is the electric component of the laser pulse in the dipole approximation. Hence, the Hamiltonian (36), excluding the term proportional to  $1/c^2$ , becomes

$$\hat{H}_{d1}(\hat{\mathbf{p}}, \hat{\mathbf{x}}, t) = \hat{H}'_1(\hat{\mathbf{p}}, t) + \hat{H}'_2(\hat{\mathbf{x}}, t) + \hat{h}'_3(\hat{\mathbf{p}}^\sigma, \hat{\mathbf{x}}^\sigma, t), \quad (43)$$

with

$$\begin{aligned} \hat{H}'_1(\hat{\mathbf{p}}, t) &= \frac{1}{2m_e} \hat{\mathbf{p}}^2, \\ \hat{H}'_2(\hat{\mathbf{x}}, t) &= \frac{1}{2m_e} [eA(t)]^2 + \frac{1}{m_e c} e^2 A(t) \mathcal{E}(t) \hat{x}_2 + V(\hat{\mathbf{x}}), \end{aligned} \quad (44)$$

and

$$\hat{h}'_3(\hat{\mathbf{p}}^\sigma, \hat{\mathbf{x}}^\sigma, t) = -\frac{e}{m_e} \left( A(t) + \frac{1}{c} \mathcal{E}(t) \hat{x}_2 \right) \cdot \hat{p}_1. \quad (45)$$

Note that, due to the properties of scheme B, it is not necessary to perform an additional unitary transformation in order to get rid of the term  $\hat{x}_2 \hat{p}_1$  in Eq. (45). Since our analysis is carried out in the inertial reference frame, in which the center of the binding potential is at rest and no noninertial forces act on photoelectrons, the interpretation of the results that follow from our numerical analysis is relatively simple. Moreover, higher nondipole terms, as well as the relativistic mass corrections, can be easily accounted for without substantial changes in the algorithm shown in scheme B.

### C. Laser pulse

In this work we limit our consideration to ionization and high-order harmonic generation driven by flat-top pulses which are smoothly turned on and off. This allows us to study, for instance, effects that are typically observed for monochromatic plane waves, provided the pulses are long enough. For example, such pulses can be described by a super-Gaussian envelope of the type  $\exp[-(t/\tau)^{N_{\text{env}}}]$ , where  $N_{\text{env}}$  is an integer much larger than 2, as this function is nearly constant for  $|t| < \tau$ . Thus, we assume that  $A(t)$  is of the form

$$A(t) = A_0 \exp \left[ - \left( \eta \frac{\omega t - \pi N_{\text{osc}}}{\pi N_{\text{osc}}} \right)^{N_{\text{env}}} \right] \sin(\omega t + \chi). \quad (46)$$

Note that the function  $A(t)$  relates not only to the electric-field strength  $\mathcal{E}(t)$ , as mentioned before, but also to the electron displacement in the laser field  $\alpha_D(t)$  [87,88],

$$\alpha_D(t) = -\frac{e}{m_e} \int_{-\infty}^t d\tau A(\tau). \quad (47)$$

In our further analysis we choose  $\eta = 1.35$  and  $N_{\text{env}} = 12$  in Eq. (46), as for such parameters  $A(t)$ ,  $\alpha_D(t)$ , and  $\mathcal{E}(t)$  vanish for  $t < 0$  and  $t > 2\pi N_{\text{osc}}/\omega$  within the accuracy of our numerical calculations. This property is illustrated in Figs. 3 and 6 below. Moreover,  $\omega$  and  $\chi$  in Eq. (46) are the carrier frequency and the carrier envelope phase of the pulse, respectively, and  $A_0$  sets up the maximum amplitude of field oscillations.

### IV. NUMERICAL DETAILS

Before investigating the nondipole signatures in ionization and high-order harmonic generation, let us first discuss some relevant details of our numerical analysis. First of all, the spatial region is defined by the parameter  $x_0$  such that  $-x_0 \leq x_1, x_2 < x_0$ . The number of points in this domain is fixed by an integer  $K$ ,

$$x_{1,j} = -x_0 + (j-1)\Delta x, \quad \Delta x = \frac{2x_0}{2^K}, \quad j = 1, \dots, 2^K, \quad (48)$$

and similarly for the second Cartesian coordinate  $x_2$ . Thus, the discretization in momentum space corresponds to

$$p_{1,j} = -\frac{\pi 2^K}{2x_0} + (j-1)\Delta p, \quad \Delta p = \frac{\pi}{x_0}, \quad (49)$$

and the same for  $p_2$ .

In order to reduce the boundary reflection effects, we introduce the mask function  $M(x)$  ( $x = \sqrt{x_1^2 + x_2^2}$ ), which is given by

$$M(x) = \begin{cases} 1, & x < r_1 \\ \left[ \cos \left( \frac{\pi}{2} \frac{x-r_1}{r_2-r_1} \right) \right]^{1/8}, & r_1 \leq x \leq r_2 \\ 0, & x > r_2, \end{cases} \quad (50)$$

with  $0 < r_1 < r_2 \leq x_0$ . This function multiplies  $\exp[-i\delta t h_2(\mathbf{x}, \bar{t}_n)]$  in scheme A (Fig. 1) as well as  $\exp[-i\frac{\delta t}{2} H_2(\mathbf{x}, \bar{t}_n)]$  in scheme B (Fig. 2). As discussed in Ref. [6], its role is equivalent to introducing an absorbing potential at the boundaries.

The wave functions  $\langle \mathbf{x}; X | \psi(t) \rangle$ ,  $\langle \mathbf{p}; P | \psi(t) \rangle$ , and  $\langle \mathbf{p}^\sigma, \mathbf{x}^\sigma | \psi(t) \rangle$  determine the probability distributions in the position and momentum spaces  $P(\mathbf{x}, t)$  and  $\tilde{P}(\mathbf{p}, t)$ , as well as in the mixed representation  $\check{P}(\mathbf{p}^\sigma, \mathbf{x}^\sigma, t)$ , respectively. The normalization of these distributions is chosen such that

$$\sum_{j=1}^{2^K} \sum_{\ell=1}^{2^K} P(x_{1,j}, x_{2,\ell}, t) (\Delta x)^2 = 1, \quad (51)$$

$$\sum_{j=1}^{2^K} \sum_{\ell=1}^{2^K} \tilde{P}(p_{1,j}, p_{2,\ell}, t) (\Delta p)^2 = 1, \quad (52)$$

and

$$\sum_{j=1}^{2^K} \sum_{\ell=1}^{2^K} \check{P}(p_j^\sigma, x_\ell^\sigma, t) \Delta p \Delta x = 1. \quad (53)$$

Note, however, that due to the leakage of probability from the finite integration region, the above normalizations are strictly fulfilled only for the initial times. With this convention, the

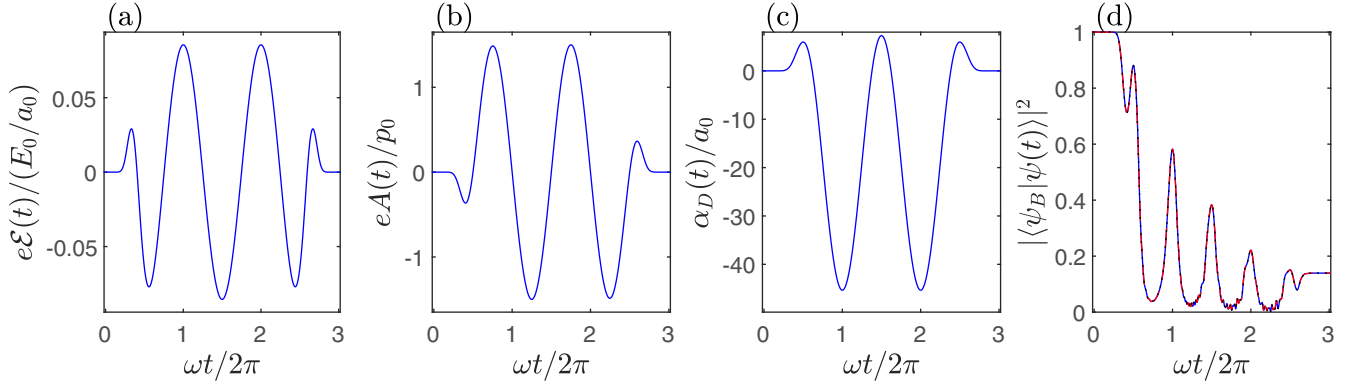


FIG. 3. Laser pulse functions for  $|e|A_0 = 1.5p_0$ ,  $\omega = 0.057E_0$ ,  $N_{\text{osc}} = 3$ ,  $N_{\text{env}} = 12$ ,  $\chi = 0$ , and  $\eta = 1.35$ : (a) electric-field strength, (b) vector potential, and (c) displacement function. For such parameters we deal with a pulse comprising one cycle in the flat-top portion of the envelope. (d) Time variation of the ground-state population for the dynamics described by the Hamiltonians (38) (full nondipole calculation, blue solid line), (41) (dipole approximation, black dotted line), and (43) (nondipole corrections, red dashed line). As we see, for these parameters the nondipole effects are hardly visible. In the numerical analysis presented here, the following parameters have been chosen (see Sec. IV):  $K = 12$ ,  $x_0 = 300a_0$ , and  $\delta t = 0.01t_0$ . For the mask function  $M(x)$  we have set  $r_1 = 280a_0$  and  $r_2 = 299a_0$ .

averages of operators  $B(\hat{x}, t)$ ,  $C(\hat{p}, t)$ , and  $D(\hat{p}^\sigma, \hat{x}^\sigma, t)$  are equal to

$$\begin{aligned} \langle B(\hat{x}, t) \rangle &= \langle \psi(t) | B(\hat{x}, t) | \psi(t) \rangle \\ &= \sum_{j=1}^{2^K} \sum_{\ell=1}^{2^K} B(x_{1,j}, x_{2,\ell}, t) P(x_{1,j}, x_{2,\ell}, t) (\Delta x)^2, \end{aligned} \quad (54)$$

$$\begin{aligned} \langle C(\hat{p}, t) \rangle &= \langle \psi(t) | C(\hat{p}, t) | \psi(t) \rangle \\ &= \sum_{j=1}^{2^K} \sum_{\ell=1}^{2^K} C(p_{1,j}, p_{2,\ell}, t) \tilde{P}(p_{1,j}, p_{2,\ell}, t) (\Delta p)^2, \end{aligned} \quad (55)$$

$$\begin{aligned} \langle D(\hat{p}^\sigma, \hat{x}^\sigma, t) \rangle &= \langle \psi(t) | D(\hat{p}^\sigma, \hat{x}^\sigma, t) | \psi(t) \rangle \\ &= \sum_{j=1}^{2^K} \sum_{\ell=1}^{2^K} D(p_j^\sigma, x_\ell^\sigma, t) \tilde{P}(p_j^\sigma, x_\ell^\sigma, t) \Delta p \Delta x, \end{aligned} \quad (56)$$

thus accounting for the depletion of probability in the integration region, as no renormalization of the wave function is applied. Moreover, the convergence of results was routinely checked by changing the parameters of the numerical analysis. In the calculation of the fast Fourier transform, we use the relevant procedures from the Intel<sup>®</sup> Math Kernel Library.

Because of the finite speed of light, we always start the time evolution at  $t_i = -x_0/c$  and end for times not smaller than  $t_f = 2\pi N_{\text{osc}}/\omega + x_0/c$ . Due to this choice, the laser pulse has not yet entered the space region for  $t < t_i$  and has already left it entirely for  $t > t_f$ .

## V. MEAN-VALUE CHARACTERISTICS OF ELECTRON WAVE PACKETS

In classical mechanics the well-known signature of nondipole effects in a linearly polarized monochromatic plane wave is the figure-eight motion of a charged particle. This shape describes a trajectory of a particle in the coordinate system in which it rests on average as well as it describes the particle acceleration, in both the plane defined by the

polarization vector and the direction of wave propagation. This property can be derived using the relativistic Hamilton-Jacobi equation [89] or the relativistic Newton equation with the Lorentz force [90]. For the latter, three invariants of motion can be obtained that determine the kinetic momentum of a particle. In the coordinate system chosen by us and neglecting the relativistic mass corrections (which are of the order of  $1/c^2$ ), these invariants lead to the relations

$$v_1(t) = -\frac{e}{m_e} A(t_r), \quad v_2(t) = \frac{1}{2c} [v_1(t)]^2, \quad (57)$$

where  $t_r = t - x_2(t)/c$ . Thus, for the acceleration vector we obtain

$$a_1(t) = \dot{v}_1(t), \quad a_2(t) = \frac{v_1(t)}{c} a_1(t). \quad (58)$$

In particular, if  $v_1(t) = v_0 \cos(\omega t_r + \phi_0)$  (with an arbitrary phase  $\phi_0$ ), then  $a_1(t) = -v_0 \omega \sin(\omega t_r + \phi_0) + O(1/c^2)$ . Hence, after squaring the second equation in (59), we arrive at the relation

$$a_2^2 = \frac{1}{c^2 \omega^2} (v_0^2 \omega^2 - a_1^2) a_1^2, \quad (59)$$

which corresponds exactly to the symmetric figure eight for the acceleration. The above derivation neglects the influence of the binding potential that can lead to some modifications of this picture, as we will discuss shortly.

In quantum mechanics the analogs of the position, velocity, and acceleration vectors are the mean values of the corresponding operators. For the position we have

$$\mathbf{x}(t) = \langle \psi(t) | \hat{\mathbf{x}} | \psi(t) \rangle. \quad (60)$$

For the velocity  $\mathbf{v}(t) = \dot{\mathbf{x}}(t)$ , depending on the choice of the Hamiltonian, we get

$$\mathbf{v}(t) = \begin{cases} \frac{1}{m_e} \langle \psi(t) | \hat{\mathbf{p}} - e\mathbf{A}(t - \frac{1}{c}\hat{x}_2) | \psi(t) \rangle & \text{for (38)} \\ \frac{1}{m_e} \langle \psi(t) | \hat{\mathbf{p}} - e\mathbf{A}(t) - \frac{e}{c} \mathcal{E}(t) \cdot \hat{x}_2 | \psi(t) \rangle & \text{for (43)} \\ \frac{1}{m_e} \langle \psi(t) | \hat{\mathbf{p}} - e\mathbf{A}(t) | \psi(t) \rangle & \text{for (41)}. \end{cases} \quad (61)$$

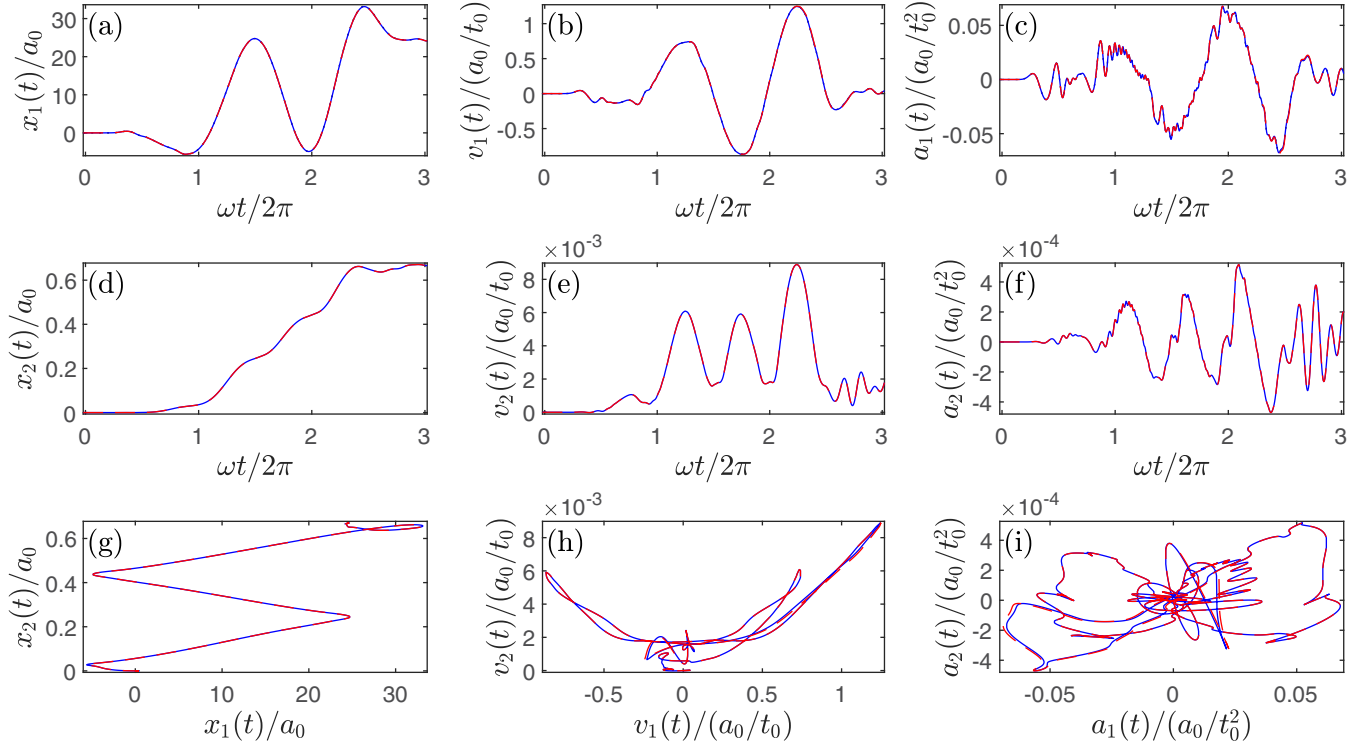


FIG. 4. Time variations of mean (a) and (d) positions, (b) and (e) velocities, and (c) and (f) accelerations for the laser pulse parameters defined in the caption of Fig. 3. (g) Relation between the mean position parallel to the laser pulse propagation direction,  $x_2(t)$ , and the mean position perpendicular to it,  $x_1(t)$ . The same relations are shown for the mean (h) velocities and (i) accelerations. We compare the mean values for three Hamiltonians: (38) (full nondipole calculation, solid blue solid line), (41) (dipole approximation, dotted black dotted line), and (43) (nondipole correction, dashed red dashed line) in panels (a), (b), and (c). Note that the black dotted lines for the dipole approximation are not visible on these plots as they exactly coincide with the other lines. In the remaining panels the comparison is made only for Hamiltonians (38) (blue solid line) and (43) (red dashed line), as in the dipole approximation the mean values parallel to the propagation direction vanish. Our results demonstrate that the lowest-order nondipole corrections to the full Hamiltonian describe the dynamics of the electron wave packet sufficiently well. In the numerical calculations, we have chosen (see Sec. IV)  $K = 12$ ,  $x_0 = 300a_0$ , and  $\delta t = 0.01t_0$  and for the mask function  $M(x)$  we have set  $r_1 = 280a_0$  and  $r_2 = 299a_0$ .

Finally, for the acceleration we use  $\mathbf{a}(t) = \dot{\mathbf{v}}(t)$ . Note that in the dipole approximation the components parallel to the propagation direction of all these vectors vanish, i.e.,  $x_2(t) = 0$ , and the same for  $v_2(t)$  and  $a_2(t)$ . Further, let us consider two cases for which the dynamics of the mean values defined above show different behavior.

#### A. Low-frequency case ( $\omega \ll |E_B|$ )

First, we consider the laser pulse of frequency  $\omega = 0.057E_0$  that corresponds roughly to the wavelength of 800 nm. In Fig. 3 we present the electric-field strength, vector potential, and displacement for the three-cycle pulse with the super-Gaussian envelope and  $|eA_0| = 1.5p_0$ . For these parameters, the ponderomotive energy equals  $U_p = e^2A_0^2/4m_e = 0.5625E_0$  and the corresponding Keldysh parameter is  $\gamma = \sqrt{|E_B|/2U_p} = 2/3$ , i.e., we consider the intermediate multiphoton-tunneling regime. In Fig. 3(d) we demonstrate the population of the ground state during the time evolution, which exhibits peaks when the modulus of the electric-field strength is maximum. It is well known that if such revivals take place, one can expect to observe the high-order harmonics in the spectrum of emitted radiation [8–11], as we will discuss shortly.

In Fig. 4 we present the mean values of the electron position, velocity, and acceleration. All these quantities in the direction of the laser pulse polarization are nearly independent of the choice of Hamiltonians considered in Sec. III B. The discrepancies appear if we consider components parallel to the pulse propagation direction, which vanish in the dipole approximation. However, if nondipole terms in the Hamiltonian are accounted for, we observe the effects related to radiation pressure that push the center of electron wave packet in the light propagation direction. The electron trajectory [Fig. 4(g)], if calculated in the reference frame of vanishing averaged velocity, resembles the figure eight, whereas the velocity dependence [Fig. 4(h)] is described quite well by the parabola (58). The discrepancies are related to the interaction (rescattering, within the classical or quantum theory) of the electron with the binding potential in the laser pulse, which is not accounted for in the classical analysis discussed above.

Even greater differences with the classical picture are manifested in the time dependence of electron acceleration, shown in Figs. 4(c) and 4(f). Here, in both cases, we observe very fast changes caused by rescattering processes. The consequence of these changes is that in the Fourier decomposition of mean values many coefficients do not disappear, which leads to the formation of a wide spectrum of high-order harmonics, as

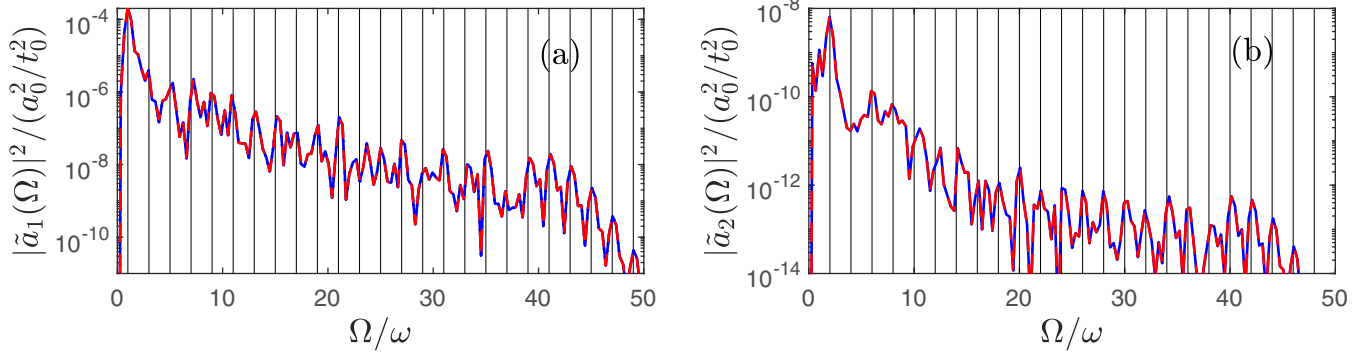


FIG. 5. Fourier transform modulus squared of the mean acceleration components which are parallel to either (a) the polarization vector or (b) the pulse propagation direction. The acceleration components are calculated for different Hamiltonians, specified by Eq. (38) (full nondipole calculation, blue solid line), Eq. (41) (dipole approximation, black dotted line), and Eq. (43) (nondipole correction, red dashed line), by numerically differentiating the mean velocity vector (61). The laser field parameters are defined in Fig. 3. The nondipole corrections due to the nonvanishing momenta of generated harmonics are smaller by two orders of magnitude. Vertical lines are for (a) odd and (b) even harmonics. Note that in both panels some harmonics are shifted towards higher energies, which is the case for short driving pulses.

presented in Fig. 5. There we observe the broad distributions of the Fourier transform modulus squared of both acceleration components which, according to the quantum analog of the Larmor formula, are proportional to the intensity of generated radiation in the leading  $1/c$  approximation (i.e., neglecting the contributions from the nonvanishing momentum of the generated photon). The cutoffs of both plateaus are given by the well-known formula [7,91]

$$\frac{\Omega_{\text{cutoff}}}{\omega} = \frac{1}{\omega} (|E_B| + 3.17U_p) \approx 40. \quad (62)$$

The nondipole signature in the high-order harmonic generation is that harmonics are also emitted in the direction of light polarization. Moreover, contrary to the “ordinary” harmonics [Fig. 5(a)], for which the spectrum consists mainly of odd harmonics, for the spectrum generated due to nondipole effects [Fig. 5(b)] we observe mostly even harmonics. A qualitative explanation of this fact can be based on the quadratic dependence of  $v_2(t)$  on  $v_1(t)$ . The latter follows directly from Eq. (58) or from Fig. 4(h), from which we can estimate that (in atomic units)  $v_2(t) \approx 2 \times 10^{-3} + [v_1(t)]^2/2c$  for times corresponding to the flat portion of the envelope. Numerical analysis of  $v_1(t)$  shows that in its Fourier decomposition the modulus squared of the constant term is around one order of magnitude smaller than the first harmonic for  $\Omega = \omega$ . Hence, since the odd harmonics dominate in the Fourier decomposition of  $v_1(t)$  and  $a_1(t)$ , in the corresponding decomposition of  $a_2(t)$  we mostly observe even harmonics. Note, however, that the analysis presented here only indicates the existence of such nondipole harmonics. Investigation of their coherent properties would require extended analysis, which is beyond the scope of this work.

In conclusion, for low-frequency laser pulses for which the Keldysh parameter  $\gamma$  is smaller than 1 (in fact, this is the most interesting case in the context of high-order harmonic generation), nondipole effects are hardly visible as long as pulses contain only a few oscillations. On the other hand, if the number of oscillations is large, the nondipole signatures are amplified at the end of the pulse, when the mean position of the electron wave packet [i.e.,  $x_2(t)$ ] is far from the potential

center and the dipole approximation (41) is no longer valid. However, this case is difficult to analyze numerically (especially for the ionization problem) because during the time evolution a significant portion of the electron wave packet leaks from the integration region. The results presented in this section agree with the existing ones, up to the even harmonics radiated in the direction of polarization. As expected, for low-frequency laser pulses the dynamics is governed mostly by the in-pulse rescattering processes. Additionally, the nondipole signatures in ionization and high-order harmonic generation by low-frequency laser fields have already been thoroughly studied in literature. For this reason, in the remaining portion of our paper, we focus on the high-frequency laser pulses, as in this case we expect to find qualitatively new results.

### B. High-frequency case ( $\omega > |E_B|$ )

The inspection of the leading-order nondipole approximation (42) shows that its validity is limited to

$$\frac{\omega}{c} |x_2(t)| \ll 1. \quad (63)$$

This condition is violated for high-frequency pulses if their intensity or the number of cycles is sufficiently large, as under such conditions the average position  $x_2(t)$  can reach a significant value at the end of the pulse. For this reason, we consider the laser pulse of frequency  $\omega = E_0$  for which  $|e|A_0 = 50p_0$ . Hence, the ponderomotive energy equals  $U_p = 625E_0$  and the Keldysh parameter is much less than one. This means that we investigate the over-barrier ionization regime in which the atom is immediately ionized by the laser field. In Fig. 6 we present the electric-field strength [Fig. 6(a)], the vector potential [Fig. 6(b)], and the displacement function for a three-cycle pulse [Fig. 6(c)]. In Fig. 6(d) the population of the ground state of a 2D hydrogen atom during the interaction with the laser field is shown. As we see, if the nondipole corrections are accounted for, the contribution of the ground state to the electron wave packet is significantly depleted just in the beginning of the pulse. In addition, the ground state is only slightly repopulated when the displacement vanishes.

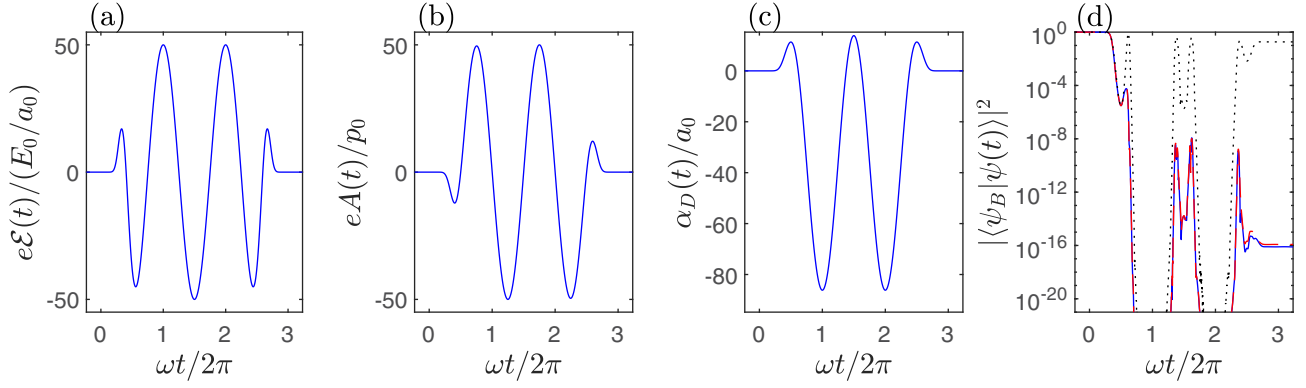


FIG. 6. Laser pulse functions for  $|e|A_0 = 50p_0$ ,  $\omega = E_0$ ,  $N_{\text{osc}} = 3$ ,  $N_{\text{env}} = 12$ ,  $\chi = 0$ , and  $\eta = 1.35$ : (a) electric-field strength, (b) vector potential, and (c) displacement function. For such parameters we deal with a pulse comprising one cycle in the flat-top portion of the envelope. (d) Time variation of the ground-state population for the dynamics described by the Hamiltonians (38) (full nondipole calculation, blue solid line), (41) (dipole approximation, black dotted line), and (43) (nondipole corrections, red dashed line). For such pulse parameters, significant nondipole effects are observed. In the numerical analysis presented here, the following parameters have been assumed (see Sec. IV):  $K = 12$ ,  $x_0 = 200a_0$ , and  $\delta t = 0.01t_0$ . For the mask function  $M(x)$  we have chosen the values  $r_1 = 180a_0$  and  $r_2 = 199a_0$ .

In order to gain deeper insight into the time evolution of the electron wave packet within the laser pulse, we now investigate the mean values. In Figs. 7(a)–7(c) we present the mean position, velocity, and acceleration in the direction of light polarization. By comparing these figures with the corresponding Figs. 6(a)–6(c) we conclude that, with very good agreement,

$$x_1(t) = \alpha_D(t), \quad v_1(t) = -\frac{e}{m_e}A(t), \quad a_1(t) = \frac{e}{m_e}\mathcal{E}(t). \quad (64)$$

This suggests that the time evolution of the electron wave packet is mainly determined by the interaction with the laser field. Hence, for the current laser pulse parameters, the rescattering with the residual ion and the Coulomb focusing effects marginally influence the mean values. The same happens also in the dipole approximation, for which the shift of the electron wave packet in the direction perpendicular to the laser pulse polarization vector is zero. For all cases considered in this paper and defined in Sec. III B, we get nearly the same dependence on time for mean values of the position, velocity, and acceleration operators, with the gradually increasing discrepancies between all of them as the pulse terminates. Moreover, for longer pulses these differences become even more significant.

The mean values of electron position, velocity, and accelerations calculated in the direction of pulse propagation are presented in Figs. 7(d)–7(f), disregarding the dipole approximation, for which all these components vanish. Here we clearly see the differences between the time evolution determined either by the full Hamiltonian (38) or by its lowest-order nondipole approximation (43). This is of course due to the large radiation pressure that moves the electron wave packet in the direction of light propagation to such an extent that the validity condition (63) is no longer applicable. The breakdown of the lowest-order nondipole approximation is clearly seen in Figs. 7(h) and 7(i). We learn from them that for the full Hamiltonian (38) the velocity  $v_2(t)$  depends quadratically on  $v_1(t)$  and for times corresponding to the flat portion of the envelope the acceleration curve adopts nearly

a perfect figure-eight shape, as follows from the classical analysis in which the interaction with the binding potential is neglected. This is another indication that just after ionization the electron wave packet moves predominantly under the action of the laser field, with apparently small corrections resulting from the interaction with the residual ion. This means that, for the current laser field parameters, the effects related to rescattering and Coulomb focusing can be disregarded while the electron is still interacting with the laser pulse.

In order to confirm the above conclusions, let us compare the quantum mean values with the classical trajectories of an electron interacting only with the laser field. To this end we have to solve the Newton equation with the Lorentz force

$$\ddot{\mathbf{x}}'(t) = \frac{e}{m_e}[\mathcal{E}(\mathbf{x}'(t), t) + \dot{\mathbf{x}}'(t) \times \mathcal{B}(\mathbf{x}'(t), t)], \quad (65)$$

where  $\mathcal{E}(\mathbf{x}', t)$  and  $\mathcal{B}(\mathbf{x}', t)$  are the electric and magnetic fields of the laser pulse. In our case, this equation reduces to the system of two ordinary differential equations

$$\begin{aligned} \ddot{x}'_1(t) &= \frac{e}{m_e c} \mathcal{E}[t - x'_2(t)/c][c - \dot{x}'_2(t)], \\ \ddot{x}'_2(t) &= \frac{e}{m_e c} \mathcal{E}[t - x'_2(t)/c]\dot{x}'_1(t), \end{aligned} \quad (66)$$

which are solved numerically with the initial conditions  $\mathbf{x}'(t = 0) = \mathbf{0}$  and  $\dot{\mathbf{x}}'(t = 0) = \mathbf{0}$ . In these equations  $\mathcal{E}(t - x'_2/c) = -\partial_t A(t - x'_2/c)$ , with the vector potential function  $A(t)$  defined by Eq. (46). Note that we distinguish the classical quantities from their quantum counterparts by adding the prime superscript. Figures 7(j)–7(l) compare the classical and quantum quantities which in fact cannot be distinguished from each other. Only by comparing the numerical values can one see the differences. For instance, for the time  $T_1 = 2\pi N_{\text{osc}}/\omega + x_0/c$ , for which the laser pulse entirely leaves the integration space, the classical values are equal to  $\mathbf{x}'(T_1) = (0, 61.6)a_0$ ,  $\dot{\mathbf{x}}'(T_1) = \mathbf{0}$ , and  $\ddot{\mathbf{x}}'(T_1) = \mathbf{0}$ . On the other hand, their quantum counterparts that also account for the binding

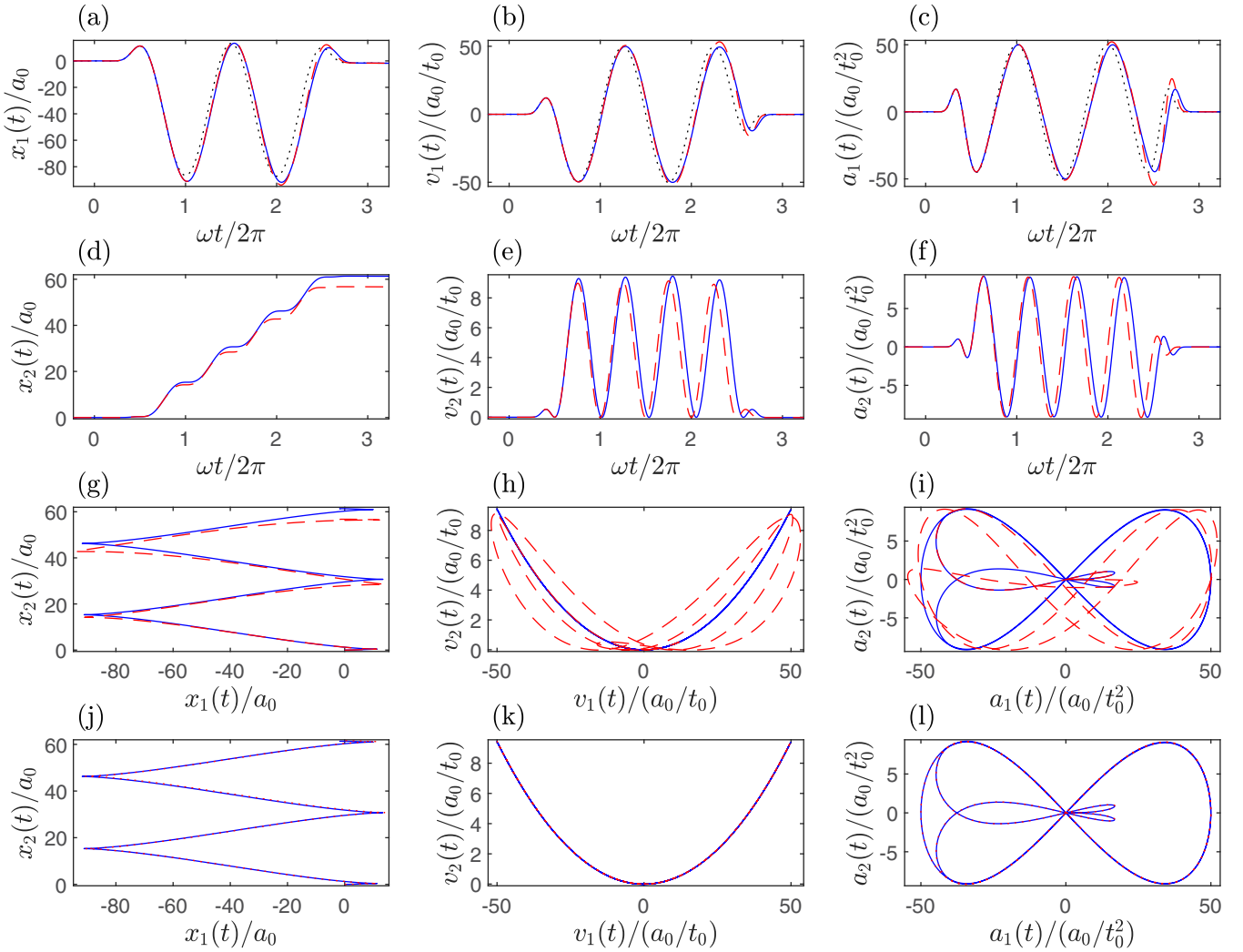


FIG. 7. Same as in Fig. 4 but for the laser pulse parameters defined in the caption of Fig. 6. For these parameters we observe discrepancies between the full Hamiltonian (38) (blue solid line) and its lowest-order nondipole approximation (43) (red dashed line). In addition, in (j)–(l) we compare the quantum mean values (blue solid line) with the classical trajectories (red dotted line) resulting from the solution of the Newton equation with the Lorentz force (65). For the full Hamiltonian, the averaged values follow very closely the classical pattern. The parameters of the numerical analysis are the same as in Fig. 6.

potential adopt the values

$$\begin{aligned} \mathbf{x}(T_1) &= (-1.8, 61.3)a_0, \quad \dot{\mathbf{x}}(T_1) = (-0.09, -0.02)(a_0/t_0), \\ \ddot{\mathbf{x}}(T_1) &= (8.2 \times 10^{-6}, -2.7 \times 10^{-4})(a_0/t_0^2). \end{aligned} \quad (67)$$

In particular, the nonvanishing acceleration is due to the Coulomb attraction, as in atomic units this vector is very close to the Coulomb force  $-\mathbf{x}(T_1)/|\mathbf{x}(T_1)|^3 = (7.8 \times 10^{-6}, -2.7 \times 10^{-4})$  [we presume that the insignificantly small difference for  $\ddot{\mathbf{x}}(T_1)$  is due to the fact that the electron probability density is distributed around the center  $\mathbf{x}(T_1)$  and/or that the acceleration has been evaluated approximately from the velocity by applying the finite-difference method]. This means that the attractive potential influences the dynamics of the quantum mean values in the pulse but for the current laser field parameters this effect is rather marginal.

## VI. ELECTRON PROBABILITY DISTRIBUTIONS

For the high-frequency case analyzed in Sec. VB we have chosen laser pulse parameters similar to the ones considered in Ref. [33]. As it follows from there, contrary to the expectations based on the radiation pressure phenomenon, a large portion of electrons is emitted opposite to the field propagation direction. Even more, the smaller the photoelectron energy is, the more emission in the opposite direction is expected. This puzzle was initially explained by considering the classical dynamics of electrons in the laser pulse and showing that the rescattering generates electron trajectories with final momenta opposite to the pulse propagation direction. This seminal work spurred further investigations of the nondipole signatures in ionization, both experimental and theoretical. In particular, it was shown that similar effects can be expected for the low-frequency fields. An expanded discussion of experimental works and theoretical models used in this context can be found in Ref. [72].

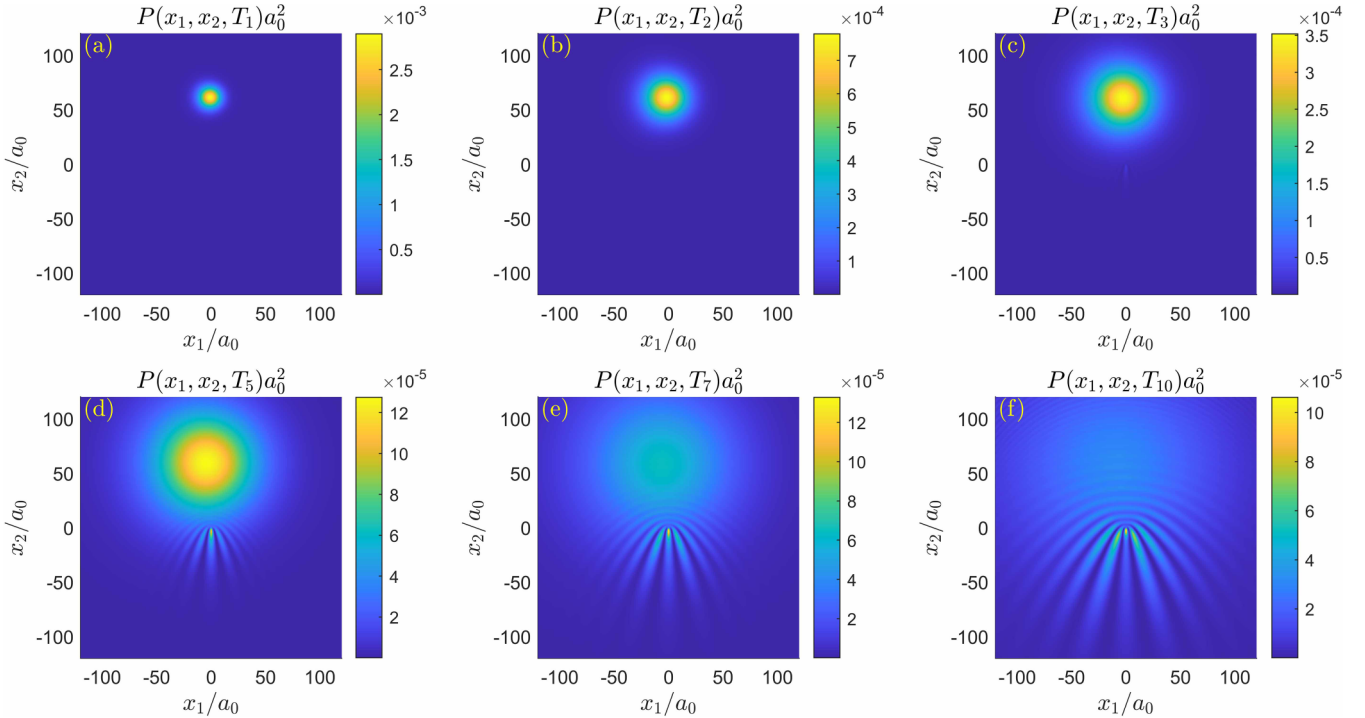


FIG. 8. Snapshots of the electron probability distribution in position space for selected times  $T_j = 2\pi j N_{\text{osc}}/\omega + x_0/c$ , for which the electron wave packet interacts only with the static binding potential. The numerical analysis has been carried out for  $x_0 = 200a_0$ ,  $\delta t = 0.01t_0$ ,  $K = 12$ , and for the mask function  $M(x)$  parameters  $r_1 = 180a_0$  and  $r_2 = 199a_0$ , as defined in Sec. IV. The laser pulse parameters are the same as in Fig. 6. The total probability for the electron wave packet to stay within the integration region is equal to 1 for  $T_1$  and 0.88 for the largest time  $T_{10}$ .

The analysis presented, for instance, in Ref. [49] shows that rescattering and Coulomb focusing in the laser field can explain the existence of electrons with negative momenta when ionized by low-frequency pulses. However, for the high-frequency fields this interpretation is in contradiction with what we discussed in Sec. VB. Therefore, yet another mechanism for the generation of photoelectrons of negative momenta (especially for energies smaller than the laser frequency) has to be proposed.

Note that the electron wave packet spreading significantly affects properties of various strong-field processes. This is due to the fact that many of them, like HHG [9,10] or generation of high-energy structures in the spectrum of emitted electrons [92], are interpreted as the result of recombination or rescattering of electrons returning to the Coulomb potential center. As long as trajectories of these electrons are determined only by their interaction with the laser field and as long as scattering is treated in the Born approximation, this picture successfully describes the aforementioned phenomena. Problems arise, however, when an attempt is made to include the electron interaction with the Coulomb field of the parent ion, e.g., in the eikonal approximation. Then, in the theoretical description, certain singularities appear that do not occur in other approaches, for example, in the Born approximation or in the numerical solution of the Schrödinger equation. As shown in Refs. [93,94], these singularities arise from neglecting the electron wave packet spreading during its interaction with the laser field which, on the other hand, is automatically accounted for in the Born series or in the generalized eikonal approximation [94].

As discussed in Sec. VB, no signatures (or marginally small signatures) of returning electrons are observed during their interaction with the high-frequency laser pulse. On the other hand, the electron wave packet also spreads after the interaction with the laser pulse is over. The aim of this section is to show that such a postpulse electron wave packet spreading together with its interaction with the parent ion leads to the formation of momentum structures for electrons moving opposite to the laser field propagation direction.

In Figs. 8 and 9 we present the snapshots of the postpulse electron wave packet distributions in the position and momentum spaces, respectively, for selected times

$$T_j = 2\pi j N_{\text{osc}}/\omega + x_0/c. \quad (68)$$

When the interaction with the laser field is over, the electron wave packet is moved far from the ionic center, with very small signatures indicating the electron scattering by the binding potential [see Fig. 8(a)]. Both position and momentum distributions are axially symmetric (exactly as the initial ground-state wave function) with the momentum distribution centered at the origin [cf. Fig. 9(a)]. From this moment on, the wave packet begins to spread, but so that its momentum distribution remains unchanged [cf. Figs. 8(b) and 9(b)]. We observe such a situation until the Coulomb field begins to noticeably affect the electron quantum dynamics. It is at this point that an interference structure in the momentum distribution of photoelectrons starts to develop due to the Coulomb focusing. As a result, a tiny local maximum (in both the position and momentum spaces) is formed for negative  $x_2$  and  $p_2$ , opposite to the radiation pressure action [cf. Figs. 8(d) and

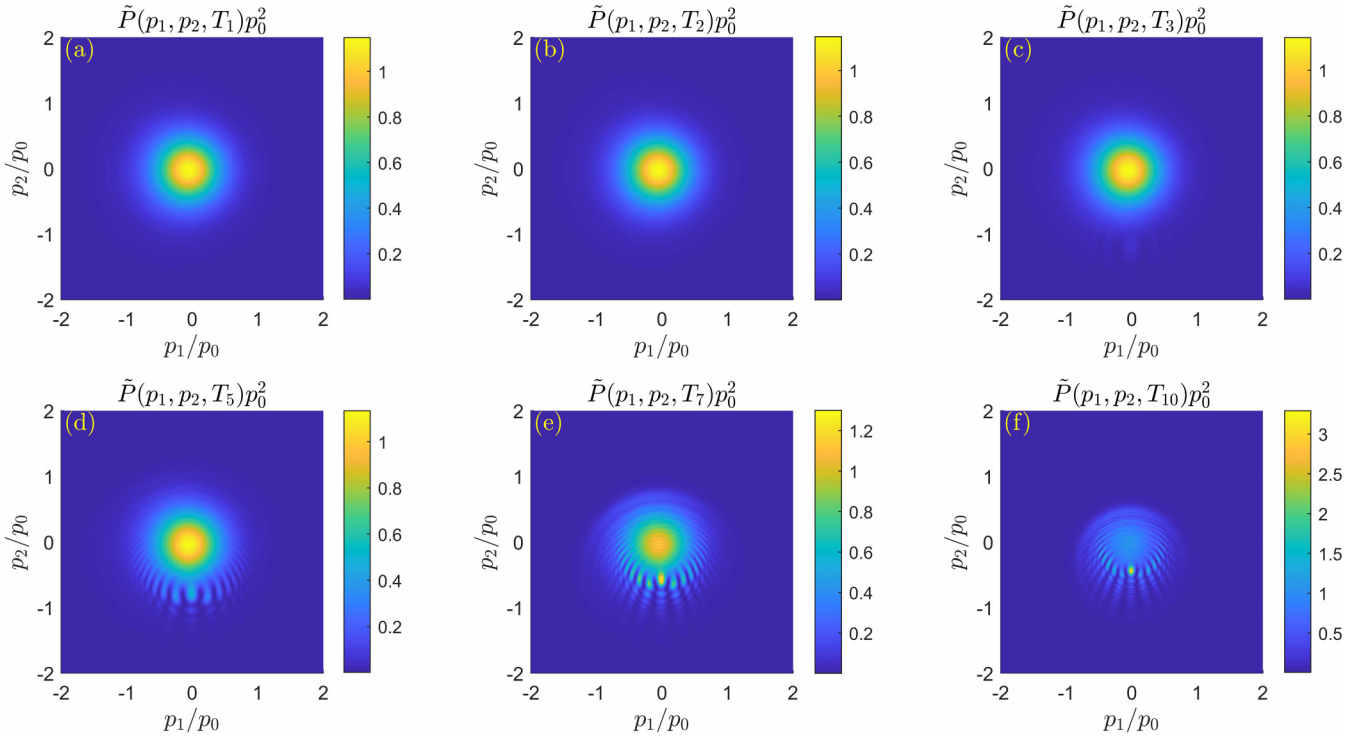


FIG. 9. Same is in Fig. 8 but in momentum space. The local maxima of these distributions are observed for  $p_1 = 0$  and for negative values of  $p_2$  equal to  $p_2 = -1.2p_0$  for  $T_3$ ,  $p_2 = -0.8p_0$  for  $T_5$ ,  $p_2 = -0.6p_0$  for  $T_7$ , and  $p_2 = -0.44p_0$  for  $T_{10}$ . Starting from  $T_7$  these are also the global maxima.

9(d)]. With time, this feature only gets enhanced, resulting eventually in a pronounced maximum located at negative momenta [cf. Figs. 9(e) and 9(f)]. Hence, we conclude that for high-frequency laser pulses, the main reasons for the backward (compared to the pulse propagation direction) shift of the electron momentum distribution is the postpulse spreading of its wave packet and the Coulomb focusing.

## VII. PROBABILITY CURRENTS

The discussion presented in Sec. VI can be continued by considering the time dependence of the electron probability current density and its flux through a surface (for the two-dimensional space this is a curve). This is what is in fact measured in experiments. However, the advantage of numerical analysis is such that one can place this surface (which can be also called the detector) very close to the studied quantum system and investigate the dynamics of the probability flow there.

The probability current density equals

$$\mathbf{j}(\mathbf{x}, t) = \frac{1}{m_e} \text{Im}[\psi^*(\mathbf{x}, t) \nabla \psi(\mathbf{x}, t)] - \frac{e}{m_e} \mathbf{A}(\mathbf{x}, t) |\psi(\mathbf{x}, t)|^2. \quad (69)$$

Next let us place the detectors on the line  $x_2 = x_D$  and orient it with the normal vector  $\mathbf{n} = \text{sgn}(x_D) \mathbf{e}_2$ , i.e., the line above the potential center is oriented in the positive  $x_2$  direction and for the line below the potential center we choose the opposite orientation. Here the function  $\text{sgn}(x)$  returns the sign of a real number  $x$ . This allows us to define the probability flux through

this line as

$$S_2(x_1, x_2 = x_D, t) = \mathbf{n} \cdot \mathbf{j}(x_1, x_2 = x_D, t). \quad (70)$$

The sign of  $S_2$  tells us in which direction the probability current density flows. In our further discussion, for visual purposes, we use the power of  $S_2$ , which is defined as  $[S_2]^p = \text{sgn}(S_2) |S_2|^p$ .

In order to investigate the convergence of our numerical scheme, we enlarge the integration space by choosing  $x_0 = 600a_0$  and setting  $K = 13$  and  $\delta t = 0.01t_0$  (see Sec. IV for the meaning of these parameters). We have checked that the results presented in Figs. 8 and 9 stay the same also for  $\delta t = 0.02t_0$ . Moreover, by defining the depletion function  $D(t)$  as

$$D(t) = \left| 1 - \int_{-x_0}^{x_0} dx_1 \int_{-x_0}^{x_0} dx_2 |\psi(x_1, x_2, t)|^2 \right|, \quad (71)$$

we find that for these new parameters  $D(T_1) < 10^{-11}$ ,  $D(T_{10}) < 5 \times 10^{-5}$ ,  $D(T_{15}) < 2 \times 10^{-3}$ , and  $D(T_{20}) < 0.012$  [and for  $x_0 = 1000a_0$  we get  $D(T_{20}) < 2 \times 10^{-4}$ ], for times  $T_j$  defined by Eq. (68). This means that the leakage of probability from the integration space is very small up to times  $T_{15}$ . These values can be read from Fig. 10(b), in which the depletion function is written in the form  $D(t) = |1 - P_+(t) - P_-(t)|$ , with  $P_{\pm}(t)$  the total probability for the electron to be found in the half plane  $x_2 > 0$  or  $x_2 < 0$  for + or -, respectively. The time dependences of these probabilities are presented in Fig. 10(a). Here we learn that the total probability for the electron to be found in the half plane  $x_2 < 0$  when the laser pulse is over is less than  $10^{-5}$  for times  $t \in [T_1, T_2]$ , i.e., practically it is zero. We arrive at the same conclusions

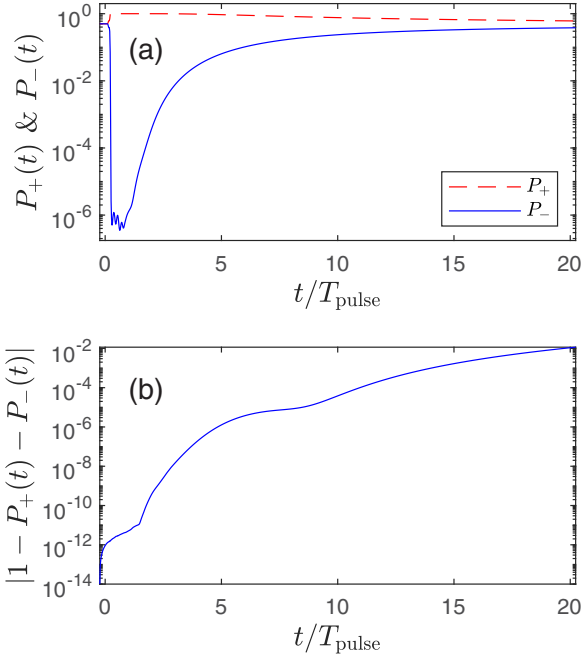


FIG. 10. (a) Time dependence of the probabilities  $P_+(t)$  (red dashed line) and  $P_-(t)$  (blue solid line) of finding the electron in the half planes  $x_2 > 0$  and  $x_2 < 0$ , respectively. We observe that at the end of the laser pulse the probability  $P_-$  is smaller than  $10^{-6}$  and then starts growing, which is due to the postpulse wave packet spreading discussed in Sec. VI. (b) Depletion function (71). In the numerical analysis presented here, the following parameters have been chosen (see Sec. IV):  $K = 13$ ,  $x_0 = 600a_0$ , and  $\delta t = 0.01t_0$ . For the mask function  $M(x)$  we have selected the values  $r_1 = 560a_0$  and  $r_2 = 599a_0$ .

for pulses with a different number of cycles and different envelopes (for instance, for the  $\sin^2$  envelope). This means that the contribution of the bound states is nearly zero for times  $t \in [T_1, T_2]$ ; thus one can assume that the state  $\psi(\mathbf{x}, T_1)$  is built up *only* of the scattering states of  $\hat{H}_{\text{at}}$ . This conclusion is further supported by the analysis of the probability current distribution discussed below.

In Fig. 11 we present the probability fluxes for five selected lines; three of them are very close to the potential center. One of them is placed at  $x_D = 10a_0$  and it needs a special discussion. In this case we present the probability flux for times when the system interacts with the laser pulse [cf. Fig. 11(a) in which, for visual purposes, the function  $S_2$  is raised to the power 1/3] and for times  $t > T_1$  [cf. Fig. 11(d)] when the pulse is over. We observe that in the laser pulse the probability flux flows in the positive  $x_2$  direction, as expected from the radiation pressure exerted on the electron cloud. The probability flux changes sign for  $t/T_{\text{pulse}} \approx 1/3$ , when the displacement of the electron wave packet in the  $x_1$  direction is maximum and the mean velocity  $v_1(t)$  changes sign. We presume that this is due to the quantum vortices created in the probability distribution (see, e.g., Ref. [14]), but a detailed exploration of this effect is beyond the scope of the present investigation. However, for later times the probability flux again changes sign such that in the middle of the pulse only a tiny fraction of the total probability (around  $10^{-5}$ ) is located below the line, i.e., in the half plane  $x_2 < 10a_0$ . Moreover, had the bound states contributed to the postpulse electron wave packet, we would have observed vortex-type structures, which are due to the circular behavior of the electron current density for bound states with nonvanishing angular momenta. Comparing Figs. 11(a) and 11(d), we see that in the time interval

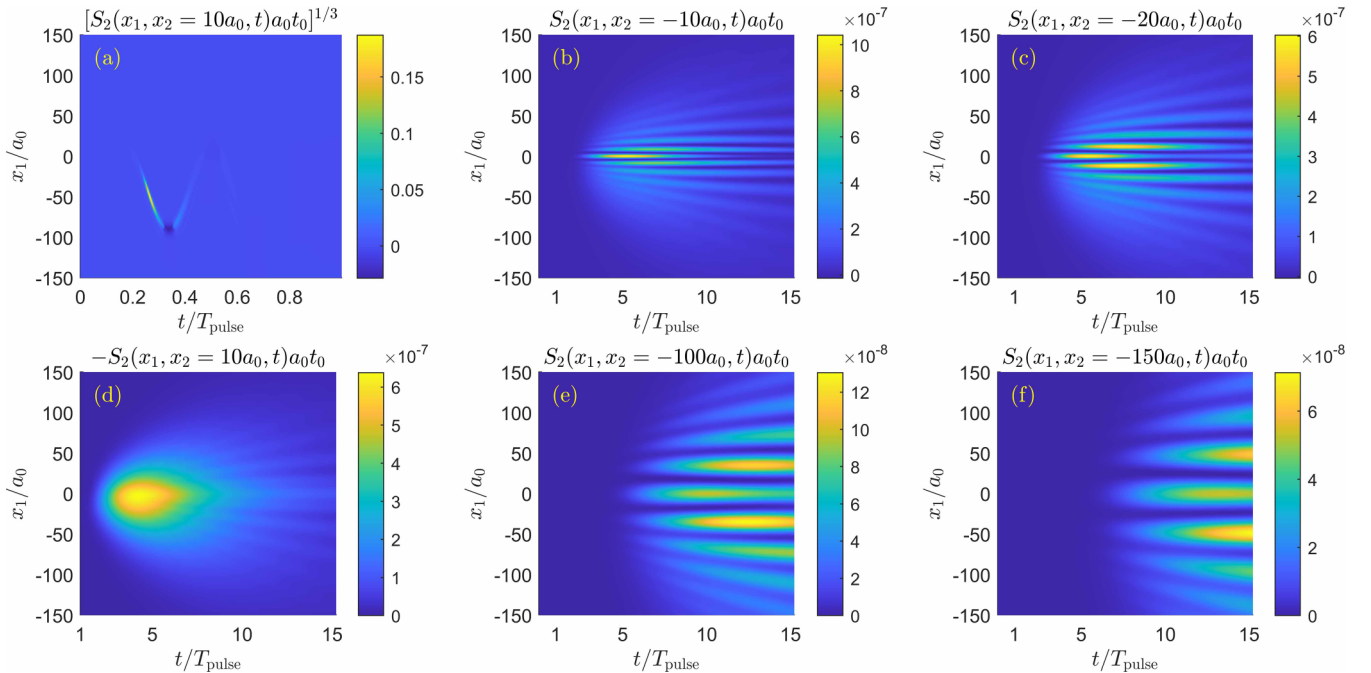


FIG. 11. Probability fluxes  $S_2(x_1, x_2 = x_D, t)$  as functions of  $x_1$  and  $t$  (in units of the pulse length  $T_{\text{pulse}} = 2\pi N_{\text{osc}}/\omega$ ) for selected lines: (a) and (d)  $x_D = 10a_0$ , (b)  $x_D = -10a_0$ , (c)  $x_D = -20a_0$ , (e)  $x_D = -100a_0$ , and (f)  $x_D = -150a_0$ . For our numerical calculations, we have chosen (see Sec. IV)  $K = 13$ ,  $x_0 = 600a_0$ , and  $\delta t = 0.01t_0$ ; for the mask function  $M(x)$ ,  $r_1 = 560a_0$  and  $r_2 = 599a_0$ .

$[T_{\text{pulse}}/2, 2T_{\text{pulse}}]$  practically no probability flux flows through the line  $x_2 = 10a_0$ . The flow reappears for  $t > 2T_{\text{pulse}}$  in the negative  $x_2$  direction and up to  $t = 7T_{\text{pulse}}$  no interference effects are observed in the distribution. A tiny interference pattern shows up for later times, which can be interpreted as the result of the postpulse backscattering of electrons by the binding potential.

A completely different pattern is observed for lines (or detectors) located below the potential center ( $x_2 < 0$ ), for which no probability flux is detected before  $t = 2T_{\text{pulse}}$ . This means that electrons in the half plane  $x_2 < 0$  cannot be created in the laser pulse (or the probability for such a process is marginally small), but appear there as the result of the postpulse dynamics. The rich interference or diffraction pattern observed here is due to the postpulse interaction of electrons with the binding potential (the so-called Coulomb focusing). These results fully support our analysis presented above and prove that the interference pattern for negative  $p_2$  momenta shown in Fig. 9 is due to the postpulse wave packet spreading and the diffraction of the electron wave on the obstacle, which in this case is the binding potential.

In conclusion, we note that one can also calculate probability fluxes for lines that are far away from the binding potential [Figs. 11(e) and 11(f)] or very close to the boundaries of the integration space. By doing this (for instance by choosing  $x_D = \pm 540a_0$  or  $\pm 500a_0$  for both  $x_1$  and  $x_2$ ), we have found that the probability fluxes are always positive and for  $t = T_{15}$  are smaller than  $10^{-9}$ . This means that the reflection of the wave packet from the boundaries vanishes or is marginally small.

### VIII. PHOTOELECTRON MOMENTUM DISTRIBUTION

In the analysis of the photoelectron momentum distribution we adopt the method used in Refs. [95–97]. The method relies on the application of the mask function (which is different from the one used for the absorption of the wave function at the boundaries), the role of which is to eliminate the contribution of bound states (if they are present) to the solution of the wave equation and to select sufficiently large momenta. To this end, let us introduce the mask function  $M_0(\bar{x})$  [ $\bar{x} = \sqrt{(x_1 - x_{c1})^2 + (x_2 - x_{c2})^2}$ ],

$$M_0(\bar{x}) = \begin{cases} 0, & \bar{x} < R_1 \\ \frac{1}{2} [1 - \cos(\pi \frac{\bar{x} - R_1}{R_2 - R_1})], & R_1 \leq \bar{x} \leq R_2 \\ 1, & \bar{x} > R_2, \end{cases} \quad (72)$$

centered around the point  $\mathbf{x}_c = (x_{c1}, x_{c2})$ .

In our further analysis we assume that  $\mathbf{x}_c = \mathbf{x}(T_1)$ , where  $\mathbf{x}(T_1)$  is the electron wave packet mean position after the pulse is over [Eq. (67)]. The smaller radius  $R_1$  has to be chosen such that the center of the binding potential lies in the interior of the circle  $|\mathbf{x} - \mathbf{x}_c| = R_1$  but sufficiently far from it. Additionally, the radius  $R_2$  cannot be too close to  $R_1$ ; otherwise the mask function  $M_0(|\mathbf{x} - \mathbf{x}_c|)$  rapidly changes its values from 0 to 1, leading to unphysical effects related to the Gibbs phenomenon (see, e.g., [98] and references therein).

Having defined the parameters of the mask function  $M_0(\bar{x})$ , a portion of the wave function  $\psi(\mathbf{x}, t)$  is selected such that it is sufficiently far away from both the initial location of the

wave packet at time  $T_1$  and the center of the binding potential, namely,

$$\psi(\mathbf{x}, t; R_1, R_2) = M_0(|\mathbf{x} - \mathbf{x}_c|)\psi(\mathbf{x}, t) \quad \text{for } t > T_1. \quad (73)$$

Next we evaluate its Fourier transform  $\tilde{\psi}(\mathbf{p}, t; R_1, R_2)$  and define the photoelectron momentum distribution

$$\tilde{P}(\mathbf{p}, t; R_1, R_2) = |\tilde{\psi}(\mathbf{p}, t; R_1, R_2)|^2. \quad (74)$$

At this point let us comment on the applicability of the adopted method. In Sec. VII we demonstrated the quantum dynamics of the electron, initially bound in the atom, that is ionized by the high-frequency laser pulse. We saw that even though the electron wave packet consists practically of only the stationary scattering states (i.e., the system is completely ionized), the process of formation of the final momentum distribution of photoelectrons is still ongoing after the pulse is over. This originates from scattering of the electron wave function by the parent ion. The scattering, although it does not change the energy distribution of photoelectrons, significantly modifies the angular distribution of emitted particles, leading to rich interference structures for probability fluxes. To account for these changes, we need to study numerically the time evolution further, but only of the electron-ion system. One can wonder for how long such an evolution should be continued. To estimate this time, let us assume that our goal is to determine the momentum distribution of photoelectrons with the momenta  $p > 0.2p_0$ . Since just after the end of the pulse, the center of the electron wave packet is at a distance of  $60a_0$  from the center of the parent ion, the time needed for electrons of such momenta to reach the ion is not smaller than  $300t_0$ , which approximately corresponds to the time  $T_{15}$ . Thus, we cannot expect that the numerically determined wave function of the electron for time  $T_{15}$  correctly defines the photoelectron momentum distribution for momenta smaller than  $0.2p_0$ , if the method used in Refs. [95–97] is applied. In order to describe the low-momentum probability distribution, the final time of the evolution should be increased appropriately, thus risking the enhancement of the probability leakage from the numerical integration area or the possibility of reflection from the boundaries. Having said that, we would like to stress that such a limitation of the adopted numerical method does not influence our main result, i.e., our interpretation of nondipole effects in high-frequency ionization that we attribute to the postpulse dynamics of the electron wave packet.

In Figs. 12(a) and 12(d) we present the electron wave packet position and momentum probability distributions, respectively, and in the remaining panels the photoelectron momentum distributions [Eq. (74)] for different choices of the mask function  $M_0(\bar{x})$ . In Fig. 12(b) the parameters  $(R_1, R_2)$  have been chosen close to each other, which leads to the creation of circular rings of small values. These are the remnants of the Gibbs oscillations present in the Fourier transform of discontinuous functions and they should not be attributed to the reflection of the wave packet from the boundaries. By increasing the distance between  $R_1$  and  $R_2$ , these unphysical features can be eliminated, as presented in Fig. 12(c). Moreover, by increasing  $R_1$  and keeping  $R_2 - R_1$  sufficiently large, we select, according to the time-of-flight rule, the part of the photoelectron distribution of larger momenta, as illustrated in Figs. 12(e) and 12(f). Let us now return to Fig. 12(d),

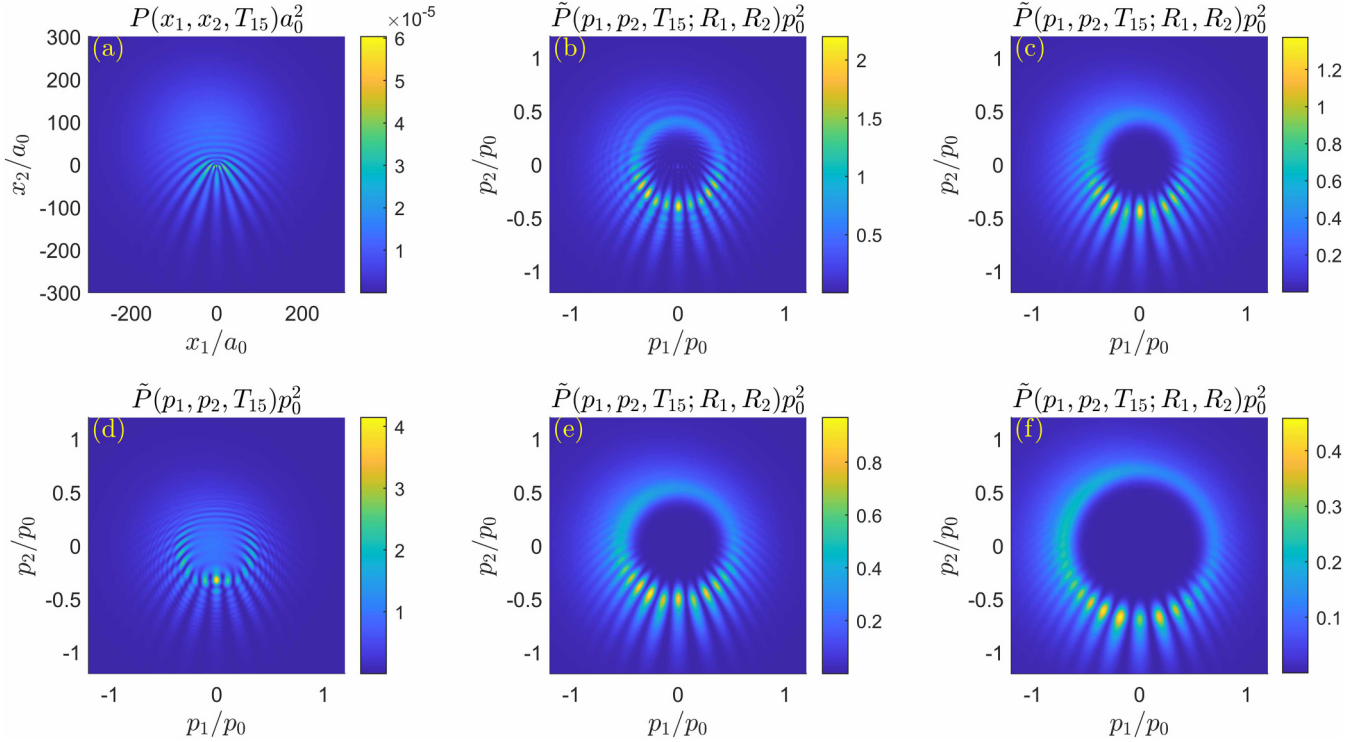


FIG. 12. Electron probability distributions in (a) position space  $P(x_1, x_2, t)$  and (d) momentum space  $\tilde{P}(p_1, p_2, t)$ , and photoelectron momentum distributions  $\tilde{P}(p_1, p_2, t; R_1, R_2)$  evaluated for  $t = T_{15} = 15 \times 2\pi N_{\text{osc}}/\omega + x_0/c$  and for different choices of  $(R_1, R_2)$ : (b)  $(80, 90)a_0$ , (c)  $(80, 130)a_0$ , (e)  $(100, 150)a_0$ , and (f)  $(150, 200)a_0$ . In accordance with the time-of-flight rule, with the increasing  $R_1$ , increasingly larger momenta are selected. In the numerical analysis, the following parameters have been chosen (see Sec. IV):  $K = 13$ ,  $x_0 = 600a_0$ , and  $\delta t = 0.01t_0$ . For the mask function  $M(x)$  we have selected the values  $r_1 = 560a_0$  and  $r_2 = 599a_0$ .

showing the modulus squared of the Fourier transform of the wave function, i.e., the momentum probability distribution. It is characterized by a close similarity to the momentum distribution of photoelectrons presented in Fig. 12(c). However, the most obvious difference is the nonvanishing probability distribution for momenta smaller than  $0.2p_0$ . In light of the above discussion, it corresponds to this part of the electron wave packet in the position space that by the time  $T_{15}$  has not yet reached the center of the binding potential and has not been scattered by it. The second difference is the notched structure for momenta greater than  $0.4p_0$ , which is the result of taking into account the wave function in the position space close to the potential center and shown in Fig. 12(a). If these particular features of the momentum distribution in Fig. 12(d) are neglected, it is qualitatively very similar to the photoelectron momentum distribution presented in Fig. 12(c).

By inspecting the photoelectron momentum distributions in Fig. 12, we observe the inner circle in which the distribution vanishes. This is due to the fact that only electrons with sufficiently large momenta can travel the distance  $R_1$  within the time  $T_{15} - T_1$ . This minimum momentum  $\check{p}(R_1)$  can be estimated by assuming that the electron moves freely from the center of the wave packet at time  $T_1$ ,

$$\check{p}(R_1) = \frac{m_e R_1}{T_{15} - T_1}. \quad (75)$$

For the chosen  $R_1$  values we get  $\check{p}(R_1 = 80a_0) = 0.3p_0$ ,  $\check{p}(R_1 = 100a_0) = 0.38p_0$ , and  $\check{p}(R_1 = 150a_0) = 0.57p_0$ .

These values suit very well the observed pattern. Additionally, there is a qualitative difference in these distributions for positive and negative  $p_2$ . Namely, for positive  $p_2$  and small  $|p_1|$  we do not observe the interference pattern, as it is the case for negative  $p_2$ . The explanation of this difference is due to the postpulse wave packet spreading (discussed in Sec. VI) and its interaction (only for negative  $p_2$ ) with the binding potential. Of course, during the wave packet spreading some electrons can be backscattered by the potential and create the interference pattern, but these are rather secondary effects, although observable in Fig. 12.

In Fig. 13 we present the one-dimensional distribution  $\tilde{P}(p_1 = 0, p_2, T_{15}; R_1, R_2)$  for three selected mask functions  $M_0(\bar{x})$ . These distributions coincide with each other for sufficiently large  $|p_2|$ . In order to estimate these limiting values of  $|p_2|$ , one can again use the time-of-flight rule for a free particle and define them as

$$\bar{p}(R_2) = \frac{m_e R_2}{T_{15} - T_1}. \quad (76)$$

Indeed, for  $|p_2| > \bar{p}(R_2 = 150a_0) = 0.57p_0$  the blue and red lines coincide with each other, whereas for  $|p_2| > \bar{p}(R_2 = 200a_0) = 0.78p_0$  all lines are nearly identical.

We observe a significant difference between the distribution for negative and positive momenta  $p_2$ , as the emission of electrons with negative momenta is strongly favored for  $p_1 = 0$ . In order to quantify this asymmetry for the entire

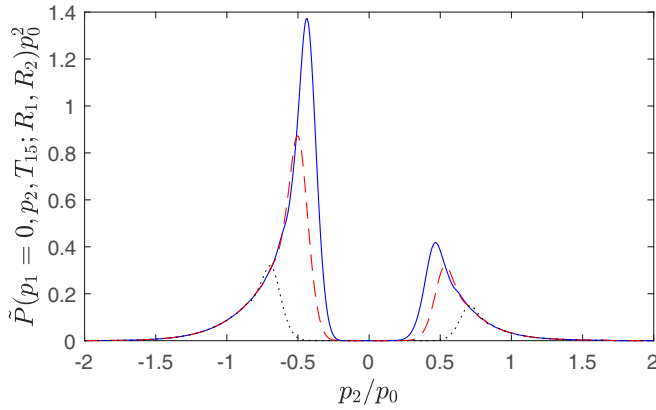


FIG. 13. Comparison of photoelectron momentum distributions presented in Fig. 12 for  $p_1 = 0$  for the following parameters  $(R_1, R_2)$  of the mask function (72):  $(80, 130)a_0$  (blue solid line),  $(100, 150)a_0$  (red dashed line), and  $(150, 200)a_0$  (black dotted line). The parameters of the numerical analysis are the same as in Fig. 12.

photoelectron distribution, we define

$$\begin{aligned}\tilde{P}_-(t; R_1, R_2) &= \int_{-q_0}^{q_0} dp_1 \int_{-q_0}^0 dp_2 \tilde{P}(\mathbf{p}, t; R_1, R_2), \\ \tilde{P}_+(t; R_1, R_2) &= \int_{-q_0}^{q_0} dp_1 \int_0^{q_0} dp_2 \tilde{P}(\mathbf{p}, t; R_1, R_2),\end{aligned}\quad (77)$$

where (see Sec. IV)  $q_0 = 2^K \pi / 2x_0$ . Thus, the asymmetry parameter at time  $t$  for a given mask function  $M_0(\bar{x})$  can be defined as the ratio

$$S(t; R_1, R_2) = \frac{\tilde{P}_-(t; R_1, R_2)}{\tilde{P}_+(t; R_1, R_2)}. \quad (78)$$

For time  $t = T_{15}$  and for mask functions considered in this section, we obtain that  $S(T_{15}; R_1, R_2) = 1.2, 1.19, 1.18$  for  $(R_1, R_2) = (80, 130)a_0, (100, 150)a_0, (150, 200)a_0$ , respectively. One can therefore see that the emission of electrons with momenta opposite to the laser pulse propagation direction is indeed more probable. This result is compatible with the postpulse dynamics of the electron wave packet from which one can expect that the absolute value of the electron mean velocity  $v_2(t)$  should increase for larger times due to the attraction of electrons by the binding potential [i.e., up to  $T_7$ , after which the absolute value of  $v_2(t)$  starts to decrease but such that during the entire postpulse time evolution  $v_2(t) < 0$ ]. Indeed,  $v_2(T_{15}) = -0.04a_0/t_0$ , compared to  $v_2(T_1) = -0.02a_0/t_0$ . [Let us note that, due to the in-pulse rescattering processes for the low-frequency case discussed in Sec. V A, the mean value  $v_2(T_1)$  is positive, as presented in Fig. 4(e). This result is consistent with other investigations.] Since, as discussed above, after the interaction with the laser pulse the electron wave packet practically consists of only

the stationary scattering states, the mean momentum  $\langle \mathbf{p} \rangle(t) = m_e \mathbf{v}(t)$  for  $t > T_1$  approximates well the mean value of the photoelectron momentum. This means that, contrary to what is expected for the low-frequency case, for the high-frequency pulse considered here, the averaged momentum  $\langle p_2 \rangle(t)$  is always negative, at least for times  $T_1 < t < T_{15}$ , for which the depletion effects are small. We checked that the change of the number of cycles in the pulse and/or of the envelope to  $\sin^2$  does not affect these conclusions.

## IX. CONCLUSION

We have introduced here the Suzuki-Trotter split-step Fourier method to solve numerically the time-dependent Schrödinger equation. It was shown that nondipole effects can be efficiently treated within this scheme. This was illustrated while studying HHG and strong-field photoionization by intense and finite laser pulses. According to our exploration, for low-frequency pulses the nondipole effects in HHG manifest as radiation emitted perpendicular to the laser field propagation direction, which is characterized by the presence of predominantly even harmonics. Furthermore, in ionization driven by high-frequency laser pulses, the radiation pressure causes a significant forward drift of the electron wave packet with negligibly small signatures related to its interaction with the binding potential (i.e., we do not observe rescattering or Coulomb focusing effects in the light field).

A surprising effect in photoionization, i.e., a backward (with respect to the pulse propagation direction) photoelectron drift, has been largely discussed (see, e.g., Refs. [33,48,49]). It was found to be caused by a modification of the electron trajectories due to Coulomb focusing. Our numerical analysis showed that, at least for the high-frequency pulses, in the description of electron dynamics one has to take into account its postpulse wave packet spreading, which is an inherently quantum phenomenon. In fact, our analysis suggested that for high-frequency laser fields the postpulse dynamics in the Coulomb field is the main cause of the electron backward shift, instead of an in-pulse trajectory modification. This interpretation is compatible with the interference structures appearing for negative momenta and a lack of them for positive momenta (with respect to the direction of the pulse propagation). Whether this mechanism also contributes to the creation of the photoelectron momentum structures for low-frequency pulses still remains an open question.

## ACKNOWLEDGMENT

This work was supported by the National Science Centre (Poland) under Grants No. 2018/30/Q/ST2/00236 (M.C.S. and K.K.) and No. 2018/31/B/ST2/01251 (F.C.V. and J.Z.K.).

- [1] P. Agostini, F. Fabre, G. Mainfray, G. Petite, and N. K. Rahman, *Phys. Rev. Lett.* **42**, 1127 (1979).  
 [2] P. A. Franken, A. E. Hill, C. W. Peters, and G. Weinreich, *Phys. Rev. Lett.* **7**, 118 (1961).

- [3] L. V. Keldysh, *Zh. Eksp. Teor. Fiz.* **47**, 1945 (1964) [*Sov. Phys. JETP* **20**, 1307 (1965)].  
 [4] F. H. M. Faisal, *J. Phys. B* **6**, L89 (1973).  
 [5] H. R. Reiss, *Phys. Rev. A* **22**, 1786 (1980).

- [6] J. L. Krause, K. J. Schafer, and K. C. Kulander, *Phys. Rev. A* **45**, 4998 (1992).
- [7] J. L. Krause, K. J. Schafer, and K. C. Kulander, *Phys. Rev. Lett.* **68**, 3535 (1992).
- [8] K. J. Schafer, B. Yang, L. F. DiMauro, and K. C. Kulander, *Phys. Rev. Lett.* **70**, 1599 (1993).
- [9] K. C. Kulander, K. J. Schafer, and J. L. Krause, in *Super-Intense Laser-Atom Physics*, edited B. Piraux, A. L'Huillier, and K. Rzażewski (Plenum, New York, 1993), p. 95.
- [10] P. B. Corkum, *Phys. Rev. Lett.* **71**, 1994 (1993).
- [11] M. Lewenstein, P. Balcou, M. Y. Ivanov, A. L'Huillier, and P. B. Corkum, *Phys. Rev. A* **49**, 2117 (1994).
- [12] D. M. Wolkow, *Z. Phys.* **94**, 250 (1935).
- [13] G. F. Gribakin and M. Y. Kuchiev, *Phys. Rev. A* **55**, 3760 (1997).
- [14] F. Cajiao Vélez, L. Geng, J. Z. Kamiński, L.-Y. Peng, and K. Krajewska, *Phys. Rev. A* **102**, 043102 (2020).
- [15] L. Geng, F. Cajiao Vélez, J. Z. Kamiński, L.-Y. Peng, and K. Krajewska, *Phys. Rev. A* **102**, 043117 (2020).
- [16] L. Geng, F. Cajiao Vélez, J. Z. Kamiński, L.-Y. Peng, and K. Krajewska, *Phys. Rev. A* **104**, 033111 (2021).
- [17] N. Grun, A. Mühlhans, and W. Scheid, *J. Phys. B* **15**, 4043 (1982).
- [18] C. Bottcher, *Phys. Rev. Lett.* **48**, 85 (1982).
- [19] N. Grun and W. Scheid, *J. Phys. B* **16**, L425 (1983).
- [20] M. Horbatsch, *J. Phys. B* **17**, 2591 (1984).
- [21] K. C. Kulander, *Phys. Rev. A* **35**, 445 (1987).
- [22] J. Javanainen, J. H. Eberly, and Q. Su, *Phys. Rev. A* **38**, 3430 (1988).
- [23] D. W. Peaceman and H. H. Rachford, *J. Soc. Ind. Appl. Math.* **3**, 28 (1955).
- [24] W. A. Murray and M. S. Lynn, *Comput. J.* **8**, 166 (1965).
- [25] H. Kono, A. Kita, Y. Ohtsuki, and Y. Fujimura, *J. Comput. Phys.* **130**, 148 (1997).
- [26] H. F. Trotter, *Proc. Am. Math. Soc.* **10**, 545 (1959).
- [27] M. Suzuki, *Proc. Jpn. Acad. B* **69B**, 161 (1993).
- [28] N. Hatano and M. Suzuki, *Lect. Notes Phys.* **679**, 37 (2005).
- [29] R. I. McLachlan, G. Reinout, and W. Quispel, *Acta Numer.* **11**, 341 (2002).
- [30] G. M. Muslu and H. A. Erbay, *Math. Comput. Simul.* **67**, 581 (2005).
- [31] M. Førre and A. S. Simonsen, *Phys. Rev. A* **90**, 053411 (2014).
- [32] M. Førre, S. Selstø, J. P. Hansen, and L. B. Madsen, *Phys. Rev. Lett.* **95**, 043601 (2005).
- [33] M. Førre, J. P. Hansen, L. Kocbach, S. Selstø, and L. B. Madsen, *Phys. Rev. Lett.* **97**, 043601 (2006).
- [34] S. Selstø, E. Lindroth, and J. Bengtsson, *Phys. Rev. A* **79**, 043418 (2009).
- [35] A. S. Simonsen and M. Førre, *Phys. Rev. A* **92**, 013405 (2015).
- [36] M. Førre and A. S. Simonsen, *Phys. Rev. A* **93**, 013423 (2016).
- [37] T. K. Lindblom, M. Førre, E. Lindroth, and S. Selstø, *Phys. Rev. Lett.* **121**, 253202 (2018).
- [38] S. Brennecke and M. Lein, *J. Phys. B* **51**, 094005 (2018).
- [39] M. Førre, *Phys. Rev. A* **106**, 013104 (2022).
- [40] C. T. L. Smeenk, L. Arissian, B. Zhou, A. Mysyrowicz, D. M. Villeneuve, A. Staudte, and P. B. Corkum, *Phys. Rev. Lett.* **106**, 193002 (2011).
- [41] H. R. Reiss, *J. Phys. B* **47**, 204006 (2014).
- [42] F. Cajiao Vélez, K. Krajewska, and J. Z. Kamiński, *Phys. Rev. A* **97**, 043421 (2018).
- [43] D. Strickland and G. Mourou, *Opt. Commun.* **56**, 219 (1985).
- [44] <https://cuos.engin.umich.edu/researchgroups/hfs/facilities/hercules-petawatt-laser/>.
- [45] V. Yanovsky *et al.*, *Opt. Express* **16**, 2109 (2008).
- [46] L. Young *et al.*, *J. Phys. B* **51**, 032003 (2018).
- [47] D. J. Wilson, A. M. Summers, S. Zigo, B. Davis, S.-J. Robotjazi, J. A. Powell, D. Rolles, A. Rudenko, and C. A. Trallero-Herrero, *Sci. Rep.* **9**, 6002 (2019).
- [48] A. Ludwig, J. Maurer, B. W. Mayer, C. R. Phillips, L. Gallmann, and U. Keller, *Phys. Rev. Lett.* **113**, 243001 (2014).
- [49] J. Maurer, B. Willenberg, J. Daněk, B. W. Mayer, C. R. Phillips, L. Gallmann, M. Klaiber, K. Z. Hatsagortsyan, C. H. Keitel, and U. Keller, *Phys. Rev. A* **97**, 013404 (2018).
- [50] M. M. Lund and L. B. Madsen, *J. Phys. B* **54**, 165602 (2021).
- [51] J. Daněk, M. Klaiber, K. Z. Hatsagortsyan, C. H. Keitel, B. Willenberg, J. Maurer, B. W. Mayer, C. R. Phillips, L. Gallmann, and U. Keller, *J. Phys. B* **51**, 114001 (2018).
- [52] M.-X. Wang, H. Liang, X.-R. Xiao, S.-G. Chen, W.-C. Jiang, and L.-Y. Peng, *Phys. Rev. A* **98**, 023412 (2018).
- [53] H. R. Reiss, *Phys. Rev. A* **42**, 1476 (1990).
- [54] K. Krajewska and J. Z. Kamiński, *Phys. Rev. A* **92**, 043419 (2015).
- [55] K. Krajewska, F. Cajiao Vélez, and J. Z. Kamiński, *J. Phys.: Conf. Ser.* **1206**, 012002 (2019).
- [56] A. Nordsieck, *Phys. Rev.* **93**, 785 (1954).
- [57] B. Böning, W. Paufler, and S. Fritzsche, *Phys. Rev. A* **99**, 053404 (2019).
- [58] B. Böning and S. Fritzsche, *J. Phys. B* **54**, 144002 (2021).
- [59] B. Böning and S. Fritzsche, *Phys. Rev. A* **106**, 043102 (2022).
- [60] S. Fritzsche and B. Böning, *Phys. Rev. Res.* **4**, 033031 (2022).
- [61] L. Rosenberg and F. Zhou, *Phys. Rev. A* **47**, 2146 (1993).
- [62] L. Rosenberg, *Phys. Rev. A* **49**, 1122 (1994).
- [63] L. Rosenberg, *Phys. Rev. A* **62**, 053401 (2000).
- [64] M. Gavril, *Phys. Rev. A* **99**, 012120 (2019).
- [65] B. Böning, W. Paufler, and S. Fritzsche, *Phys. Rev. A* **101**, 031401(R) (2020).
- [66] M. Klaiber, K. Z. Hatsagortsyan, and C. H. Keitel, *Phys. Rev. A* **105**, 053107 (2022).
- [67] P.-L. He, M. Klaiber, K. Z. Hatsagortsyan, and C. H. Keitel, *Phys. Rev. A* **105**, L031102 (2022).
- [68] D. Habibović and D. B. Milošević, *Phys. Rev. A* **106**, 033101 (2022).
- [69] S. Chelkowski, A. D. Bandrauk, and P. B. Corkum, *Phys. Rev. Lett.* **113**, 263005 (2014).
- [70] M.-X. Wang, X.-R. Xiao, H. Liang, S.-G. Chen, and L.-Y. Peng, *Phys. Rev. A* **96**, 043414 (2017).
- [71] M.-X. Wang, H. Liang, X.-R. Xiao, S.-G. Chen, and L.-Y. Peng, *Phys. Rev. A* **99**, 023407 (2019).
- [72] N. Haram, R. T. Sang, and I. V. Litvinyuk, *J. Phys. B* **53**, 154005 (2020).
- [73] E. Hairer, C. Lubich, and G. Wanner, *Geometric Numerical Integration. Structure-Preserving Algorithms for Ordinary Differential Equations* (Springer, Berlin, 2006).
- [74] C. Skokos, E. Gerlach, J. D. Bodyfelt, G. Papamikos, and S. Eggl, *Phys. Lett. A* **378**, 1809 (2014).
- [75] M. Suzuki, *Phys. Lett. A* **146**, 319 (1990).
- [76] H. Yoshida, *Phys. Lett. A* **150**, 262 (1990).
- [77] J. W. Cooley and J. W. Tukey, *Math. Comput.* **19**, 297 (1965).
- [78] P. O. J. Scherer, *Computational Physics: Simulation of Classical and Quantum Systems* (Springer, Cham, 2017).

- [79] D. Takahashi, *Fast Fourier Transform Algorithms for Parallel Computers* (Springer, Singapore, 2019).
- [80] A. D. Bandrauk and H. Shen, *J. Chem. Phys.* **99**, 1185 (1993).
- [81] H. Bauke and C. H. Keitel, *Comput. Phys. Commun.* **182**, 2454 (2011).
- [82] T. Dziubak and J. Matulewski, *Comput. Phys. Commun.* **183**, 800 (2012).
- [83] Y. Fu, J. Zeng, and J. Yuan, *Comput. Phys. Commun.* **210**, 181 (2017).
- [84] J. Derlikiewicz, *Dynamics of two-dimensional quantum systems interacting with short laser pulses*, M.Sc. thesis, University of Warsaw, 2022, available at [https://www.fuw.edu.pl/~jderlikiewicz/mgr/mgr\\_JD.pdf](https://www.fuw.edu.pl/~jderlikiewicz/mgr/mgr_JD.pdf).
- [85] K. Liu, Y. Hu, Q. Zhang, and P. Lu, *Opt. Express* **29**, 38758 (2021).
- [86] Y. Hu, K. Liu, Q. Ma, and P. Lu, *J. Opt. Soc. Am. B* **39**, 2486 (2022).
- [87] W. C. Henneberger, *Phys. Rev. Lett.* **21**, 838 (1968).
- [88] N. M. Kroll and K. M. Watson, *Phys. Rev. A* **8**, 804 (1973).
- [89] L. D. Landau and E. M. Lifshitz, *The Classical Theory of Fields* (Pergamon Press, Oxford, 1971).
- [90] F. Cajiao Vélez, J. Z. Kamiński, and K. Krajewska, *J. Phys.: Conf. Ser.* **999**, 012007 (2018).
- [91] C. J. Joachain, N. J. Kylstra, and R. M. Potvliege, *Atoms in Intense Laser Fields* (Cambridge University Press, Cambridge, 2012).
- [92] D. B. Milošević, G. G. Paulus, D. Bauer, and W. Becker, *J. Phys. B* **39**, R203 (2006).
- [93] F. Cajiao Vélez, K. Krajewska, and J. Z. Kamiński, *Phys. Rev. A* **91**, 053417 (2015).
- [94] J. Z. Kamiński, F. Cajiao Vélez, and K. Krajewska, *J. Phys.: Conf. Ser.* **1206**, 012004 (2019).
- [95] M. Spanner, S. Gräfe, S. Chelkowski, D. Pavičić, M. Meckel, D. Zeidler, A. B. Bardon, B. Ulrich, A. D. Bandrauk, D. M. Villeneuve, R. Dörner, P. B. Corkum, and A. Staudte, *J. Phys. B* **45**, 194011 (2012).
- [96] S. Chelkowski, A. D. Bandrauk, and P. B. Corkum, *Phys. Rev. A* **92**, 051401(R) (2015).
- [97] M.-Y. Ma, J.-P. Wang, W.-Q. Jing, Z. Guan, Z.-H. Jiao, G.-L. Wang, J.-H. Chen, and S.-F. Zhao, *Opt. Express* **29**, 33245 (2021).
- [98] D. Kanti, J. Z. Kamiński, L.-Y. Peng, and K. Krajewska, *Phys. Rev. A* **104**, 033112 (2021).